






# Enhancing Dynamic Performance of Islanded Microgrids by Fractional-Order Derivative Droop

Amr M. AbdelAty , Senior Member, IEEE, Ahmed Al-Durra , Senior Member, IEEE, Hatem H. Zeineldin , Senior Member, IEEE, Saikrishna Kanukollu , Member, IEEE, and Ehab F. El-Saadany , Fellow, IEEE

**Abstract**—Islanded operation of microgrids (MGs) with parallel-operated inverters imposes many control challenges in terms of stability and dynamic behavior, especially at contingency events. Hence, improving the dynamic performance and the stability margin is essential for robust MG operation. Therefore, the fractional-order derivative (FOD) droop controller is proposed to achieve these goals. A detailed small signal model is developed for the entire MG with the proposed controller and then used to assess the stability of the MG. The FOD and the integer-order derivative (IOD) droop controllers are applied to a benchmark MG and tuned via an optimization procedure under multiple loading conditions. The results show that the extra degrees of freedom introduced by the FOD droop facilitate pushing the dominant modes toward the required stability region. The proposed FOD droop is compared to the IOD droop, conventional droop, VOC, and virtual synchronous generator controllers under several contingency events and a reconfiguration scenario using MATLAB/SIMULINK, where the proposed controller shows superior performance. The experimental validations demonstrate the improved power-sharing performance of the proposed FOD droop controller.

**Index Terms**—Derivative droop, droop control, fractional control.

Manuscript received 10 September 2023; revised 29 November 2023 and 13 February 2024; accepted 4 March 2024. Date of publication 17 April 2024; date of current version 2 July 2024. This work was supported by Khalifa University under Grant CIRA-013-2020 and Grant CIRA-2021-063. Paper no. TII-23-3477. (Corresponding author: Amr M. AbdelAty.)

Amr M. AbdelAty is with the Advanced Power and Energy Center, Khalifa University of Science Technology, Abu Dhabi 127788, UAE, and also with the Engineering Mathematics and Physics Department, Fayoum University, Fayoum 63514, Egypt (e-mail: ama51@fayoum.edu.eg).

Ahmed Al-Durra is with the Electrical and Computer Engineering, Khalifa University of Science Technology, Abu Dhabi 127788, UAE (e-mail: ahmed.aldurra@ku.ac.ae).

Hatem H. Zeineldin is with the Advanced Power and Energy Center, Khalifa University of Science Technology, Abu Dhabi 127788, UAE, and also with the Electric Power Engineering Department, Cairo University, Giza 12613, Egypt (e-mail: hatem.zeineldin@ku.ac.ae).

Saikrishna Kanukollu is with Khalifa University, Abu Dhabi 127788, UAE (e-mail: saikrishna.kanukollu@ku.ac.ae).

Ehab F. El-Saadany is with the Advanced Power and Energy Center, Khalifa University of Science Technology, Abu Dhabi 127788, UAE (e-mail: ehab.elsadaany@ku.ac.ae).

Color versions of one or more figures in this article are available at <https://doi.org/10.1109/TII.2024.3378802>.

Digital Object Identifier 10.1109/TII.2024.3378802

## I. INTRODUCTION

MICROGRIDS (MGs) have proven to be a feasible alternative to adjusting the existing grid networks to cope with the increasing energy demands [1], [2], [3]. This is because, in MGs, long transmission lines are avoided by placing the generation closer to the demand. Dispatchable sources, such as diesel generators, and nondispatchable sources, such as PV and wind, are deployed in MGs and termed distributed generation (DG). These DGs are interfaced through power electronic converters, which are classified based on their operation mode into grid following and grid forming inverters [4]. In the islanded mode of operation, a MG has to operate independently and maintain its own voltage and frequency locally [5]. However, MGs suffer from lower inertia compared with traditional power systems due to the absence of rotating mass and the higher penetration of inverter-based resources (IBRs). So, the modeling, control, and stability improvement of parallel-operated inverters in islanded MGs have attracted the attention of many researchers.

In islanded MGs, many of the control methods employed for controlling the parallel operation of inverters are inherited from the behavior and control techniques of synchronous generators (SGs). Active power oscillation is a known disadvantage of parallel SGs. Yet, SGs have good overload capabilities, which makes these power oscillations not a critical problem. However, for parallel inverters, the power electronic switches have limited overcurrent ratings, and such power oscillations can damage these switches and lead to unsafe system operation during load transients [6]. So, many techniques have been proposed to improve the transient dynamics of power oscillations without affecting the steady-state active power-sharing performance. In [6], improved damping of the active power oscillations was approached by adjusting the virtual stator reactance to achieve approximately equal total output per unit reactance between connected virtual synchronous generators (VSGs), which led to an increased active power-sharing damping ratio. A power oscillation suppression control strategy was proposed in [7] for the case of parallel synchronverters via virtual damping term (for response speed) and virtual impedance (for oscillations reduction). Acceleration control via frequency derivative feedback and disturbance compensation via the derivative of active power feedback were used as a damping strategy for power oscillation in parallel VSGs [8]. The time derivative of active power was used in a decentralized mutual damping control

scheme for parallel VSGs [9]. The experimental results showed an improved settling time (ST) of active power oscillations, but the overshoot was only slightly improved compared to the conventional VSG method. A virtual oscillator frequency locked loop was proposed to estimate grid frequency and implement local friction damping torque to diminish power oscillations in parallel connected virtual synchronous machines [10]. A mutual damping control scheme was proposed for a consensus algorithm incorporated with a model predictive controller to reduce power oscillation at load disturbance in the case of multi-VSG islanded MG [11]. A center of inertia estimator was implemented in a distributed control scheme for multi-VSG grids to reduce power and frequency oscillations and improve dynamic performance [12]. A decentralized transient damping controller, which created two extra degrees of freedom, was used to suppress power oscillations in parallel VSG systems during load transients [13].

Droop control is a type of decentralized primary control, which is dominant in MG control due to its simplicity, ease of installation, and operation without communication links. It resembles the operation of synchronous generators in traditional power systems. However, it is known to show oscillatory response and a small stability margin, especially at the increasing number of grid-forming inverters [14]. The stability margin was increased using a series of lead compensators in the  $P$ - $f$  droop control loop, where two stages were enough to triple the value of the maximum active droop gain [15]. A modified power measurement filter was proposed in the conventional droop controller to eliminate the effects of the distribution system lag factor and the EM induced coupling and damping, and it showed an increase in the stability margin [16]. The interaction between droop-controlled inverters through the power network was studied in [17], where a robust  $H_\infty$  controller was used to suppress the low-frequency oscillations and act as a replacement for the virtual impedance loop. An inner-loop disturbance observer controller combined with a  $V$ - $I$  droop controller was introduced to address the impacts of feeder impedance and PCC voltage variations on active and reactive power sharing [18]. A domain-enriched optimization algorithm was proposed to improve the dynamics of islanded droop-controlled MGs [19]. The optimization problem aimed at finding the best controller parameters using an eigenvalues-based fitness function. A dynamic droop controller was proposed to address the transient power-sharing in islanded MGs [20]. The controller involved a differential control loop consisting of a bandpass filter, a proportional derivative controller, and a damping loop, which is a highpass filter. Adaptive droop coefficients, based on output currents, were proposed for conventional droop control to enhance transient and steady-state power-sharing in stand-alone MGs [21]. However, the proposed controller induced power-sharing oscillations in some of the studied cases while improving overshoot.

A PID/PD droop controller was proposed in [22] to improve the transient response of single-phase parallel-operated inverters. This controller had the same steady-state performance as the conventional  $P$ - $f/Q$ - $V$  droop while being able to adjust the dynamic response via proper tuning of the new controller's gains. Similarly, a PD/PD droop controller was proposed for the  $P$ - $V/Q$ - $f$  droop controller used in low voltage

single-phase MGs with resistive line impedance [23]. A PD/PD droop control scheme in  $dq$  frame was proposed for the first time for 3-phase parallel-operated inverters in [24]. The derivative droop gains, seen as extra degrees of freedom, were scheduled through small-signal analysis to maintain a particular transient response irrespective of the loading condition. After that, the PD droop, also known as the derivative droop, has been used inside larger control structures as the control part that provides a more stable and robust performance of power-sharing dynamics. A control scheme was proposed for MG converters in [25] that is composed of an  $\alpha$ - $\beta$  frame voltage controller and the derivative droop controller. The gains of the derivative droop were optimized using PSO based on the transient response of the power-sharing dynamics at multiple MG operating conditions and contingency events. The derivative droop controller was compared with the conventional droop controller, and it showed an improved response in several aspects, including the circulating current transients. The whole cycle adaptive droop was proposed in [26], which is an adaptive and nonlinear version of the derivative droop where the derivative gains are functions of the active/reactive powers and their derivatives. The controller was used, in conjunction with virtual impedance and improved power calculation, in an auxiliary parallel system to mitigate the trade-off between voltage regulation and active power sharing in  $P$ - $V/Q$ - $f$  droop. The derivative droop was used in a hybrid cost-based droop control to achieve optimal generation while maintaining an improved stability margin [27]. The stabilizing impact of the reactive droop and reactive derivative droop was intensively studied in [28]. It was revealed that the derivative droop in the reactive path alone is capable of improving MG stability while sustaining equal power sharing.

Based on the above, the literature on power oscillation suppression mechanisms in islanded MGs is oriented toward multi-VSG and VSM-based MGs, with limited consideration for droop-based MGs despite the prevalence of the droop controller in practice. Also, it is evident that the derivative droop is a suitable controller for improving the damping of the power-sharing dynamics, as its overshoot and ST are better than the conventional droop controller. IOD droop achieves that without affecting the steady-state characteristic, making it and similar approaches excellent retrofits for the widely used droop controller. However, it has some limitations exemplified as the tradeoff between power-sharing speed and overshoot, as analyzed in Section II. Nevertheless, any further improvement in IOD droop dynamic response requires extra degrees of freedom, which can be provided using fractional order controls. To the best of our knowledge, the fractional-order version of the derivative droop controller has not been studied in the literature despite the proven advantages of FO controllers in improving MG dynamics compared with the IO controllers. For example, an adaptive fractional-order grid frequency controller was recently proposed for the doubly fed induction generator wind turbine [29]. A FOD of the grid frequency of order between 1 and 2 was used in the inertia controller. A fractional order of 1.3 was recommended, where the frequency drop and fluctuations are at their minimum based on a simulated real grid from Ontario, Canada. This promising result and many others have motivated the authors to study the FOD droop and compare its performance against the

**TABLE I**  
LIST OF ACRONYMS AND THEIR DEFINITIONS

Acronym	Definition
MG	Microgrid
DG	Distributed Generation
VSC	Voltage Source Converter
VSG	Virtual Synchronous Generator
VOC	Virtual Oscillator Control
SG	Synchronous Generator
EM	Electromagnetic
IO	Integer Order
FO	Fractional Order
IOD	Integer Order Derivative
FOD	Fractional Order Derivative
FOC	Fractional Order Control
LPF	Low Pass Filter
SSM	Small Signal Model

conventional droop controller, the original IOD droop, and VOC and VSG, which are two recent grid-forming controller schemes. The proposed controller is carefully analyzed from a theoretical perspective, and a detailed implementation is given. The FOD droop shows enhancement in different aspects of power-sharing dynamics, as illustrated through multiple simulations as well as experimental case studies.

The contributions of this work can be summarized as follows.

- 1) Improving the transient response of the power-sharing dynamics using FOD droop, which leads to an increased stability margin, a more robust response, and a reduction of stresses on the power electronic switches in the case of several tested contingency events and hardware validations.
- 2) Developing a method to realize biproper transfer function approximations of the fractional-order operator  $s^\gamma$  without affecting other integer order states.
- 3) Provide the complete SSM of the MG under the proposed controller, which is then used to obtain the eigenvalues of the system and tune the controller.

Table I summarizes the acronyms used in the article, and the rest of this article is divided into multiple sections as follows. Section II provides a simplified small signal analysis of power oscillation mechanisms for parallel-operated VSCs and compares the performance of the proposed FOD droop, IOD droop, conventional droop, and VSG control. Section III discusses the proposed controller and provides a detailed small signal analysis of FOD droop-controlled MG. Section IV contains the simulation verification of the proposed controller, its proposed tuning method, and its comparison with other grid-forming controllers under multiple disturbance events. Section V is dedicated to the sensitivity analysis of the proposed controller gains and orders and the proposed controller's performance under the uncertainty of several MG parameters. The experimental validation of the proposed controller is discussed in Section VI on a Lab-scale MG.

## II. POWER OSCILLATION MECHANISM OF PARALLEL VSCS

### A. Fractional-Order Calculus Preliminaries

Fractional calculus is a recently rediscovered mathematical tool that has drawn the inquisitiveness of many researchers

due to its flexibility in modeling and control of dynamical systems [30]. It deals with models described by noninteger order integrals and derivatives, so it is a generalization of the traditional integer order modeling and control methods. The extra degrees of freedom emitting from the new fractional orders parameters have been shown to provide better representations of real-world phenomena and achieve better control performance that was simply unattainable with the traditional integer order tools [31], [32].

Within the scope of fractional-order control, efficient approximations of the fractional-order operators (integrals or derivatives) are needed for practical realization purposes [33], [34], [35], [36]. Also, these approximations enable the use of well-accepted integer order simulation software and stability assessment methods when designing FO controllers. These approximations are either based on time or frequency domain resemblance to the ideal fractional order operator but with more focus on the operating requirement of interest. Frequency domain approximations are designed to emulate the magnitude and frequency responses of  $s^\gamma$  within a predetermined frequency range, which is chosen to track the important dynamics of the fractional-order controller [37]. In this work, the Matsuda approximation is adopted and realized with the help of FOTF toolbox [38]. The convergent number of the continued fraction form of the Matsuda approximation is chosen so that the output transfer function has an equal number of poles and zeros, as follows:

$$s^\gamma \approx G_\gamma(s) = \frac{\sum_{k=0}^N \hat{a}_k s^k}{\sum_{k=0}^N \hat{b}_k s^k}, -1 < \gamma < 1. \quad (1)$$

### B. Power Oscillation Analysis

Active power oscillation is an unavoidable phenomenon of parallel-operated VSCs. Hence, in this section, the effect of load disturbance on the active power oscillations is analyzed for the case of two parallel-operated inverters under derivative droop control. The same modeling procedure for parallel operated VSGs discussed in [39] is adopted here, however, for FOD droop control. The active power droop relation for an inductive system is written as follows:

$$\omega = \omega_n - \frac{m_p \tilde{p}}{\tau_c s + 1} \quad (2)$$

where  $\tilde{p}$  is the unfiltered active power,  $\tau_c$  is the time constant of the low-pass filter used to average the measured power,  $m_p$  is the active droop gain, and  $\omega_n$  is the nominal frequency of the MG. The proposed FOD active power droop controller is given as follows:

$$\omega = \omega_n - \frac{m_p \tilde{p}}{\tau_c s + 1} - \frac{m_d s^\alpha \tilde{p}}{\tau_{c,d} s + 1}. \quad (3)$$

where  $m_d$  is the derivative droop gain, and  $\alpha \in (0, 2)$  is the derivative droop fractional order. Note that when  $\alpha = 1$ , (3) corresponds to the IOD droop proposed in [24].

This section assumes that  $\tau_{c,d} = \tau_c$  to simplify the analysis. Hence, the FOD droop control relation for the  $i$ th inverter can

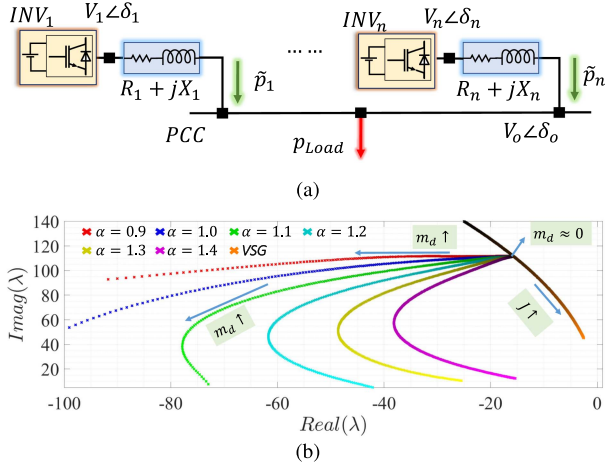


Fig. 1. (a) Parallel VSCs. (b) The poles locus of  $\frac{\Delta \tilde{p}_i}{\Delta p_{load}}$  for FOD droop-controlled VSCs at different  $\alpha$  for  $m_d \in [0, 10^{-5}]$  and for VSG-controlled VSCs for  $J \in [0.1, 1]$ .

be rewritten as follows:

$$\omega_i = \omega_n - \frac{(m_p + m_d s^\alpha)}{(\tau_c s + 1)} \tilde{p}_i \quad (4)$$

where  $\tau_c = 1/\omega_c$ . The perturbation of the active power output of the  $i$ th VSC at load disturbance can be expressed as follows:

$$\Delta \tilde{p}_i = \frac{V_i V_o}{X_{i0}} \cos(\delta_i^0 - \delta_o^0) (\Delta \delta_i - \Delta \delta_o) = k_{i0} (\Delta \delta_i - \Delta \delta_o) \quad (5)$$

where  $V_i$ ,  $V_o$ ,  $X_{i0}$ ,  $\delta_i$ , and  $\delta_o$  are as depicted in Fig. 1(a). Also,  $\Delta \delta_i - \Delta \delta_o = \frac{1}{s} (\Delta \omega_i - \Delta \omega_o)$ , where  $\Delta \omega_o$  is the frequency perturbation at PCC. Based on the above relations, one can derive the formula

$$\Delta \tilde{p}_i = \frac{-k_{i0} (\tau_c s + 1) \Delta \omega_o}{\tau_c s^2 + s + m_d k_{i0} s^\alpha + m_p k_{i0}} = H_i(s) \Delta \omega_o. \quad (6)$$

Using the power balance relation:  $\sum_{i=1}^n \Delta \tilde{p}_i = \Delta p_{load}$ , the following can be derived for the general case of  $n$  inverters and two inverters, respectively.

$$\frac{\Delta \tilde{p}_i}{\Delta p_{load}} = \frac{H_i(s)}{\sum_{i=1}^n H_i(s)} \quad (7a)$$

$$\frac{\Delta \tilde{p}_2}{\Delta p_{load}} = \frac{k_{20} (\tau_c s^2 + s + m_d k_{10} s^\alpha + m_p k_{10})}{2\tau_c s^2 + 2s + m_d s^\alpha (k_{10} + k_{20}) + m_p (k_{10} + k_{20})}. \quad (7b)$$

The poles locus of (7b) are illustrated in Fig. 1(b) for different  $\alpha$  (including the integer case at  $\alpha = 1$ ), and for  $m_d \in [0, 10^{-5}]$  for the condition  $k_{10} \neq k_{20}$ . The operator  $s^\alpha$  is emulated using the Matsuda approximation. For VSG control, the transfer function  $\frac{\Delta \tilde{p}_2}{\Delta p_{load}}$  is as derived in [39], and its pole trajectory is also shown in Fig. 1(b) for varying the inertia coefficient  $J \in [0.1, 1]$  and a fixed damping coefficient of  $D_p = 1/m_p = 1592 \text{ W}\cdot\text{s}/\text{rad}$ . This value of  $D_p$  is chosen so that VSG, droop, IOD droop, and FOD droop have similar steady-state characteristics. In Fig. 1(b), all FOD droop curves start from the same point at  $m_d \approx 0$ , which corresponds to the conventional droop control. As  $m_d$  increases,

the trajectory of the poles is dependent on the choice of  $\alpha$ , and it is evident that poles corresponding to  $\alpha > 1$  have a better damping ratio  $\zeta$  than the poles corresponding to  $\alpha \leq 1$  at the same real part of the pole ( $\sigma$ ). For VSG control, increasing  $J$  improves  $\zeta$  but decreases  $\sigma$ . So, requirements on both can not be satisfied with VSG control unless steady-state characteristics are modified via  $D_p$ .

In conclusion, the IOD droop has only one tuning parameter ( $m_d$ ), and its pole trajectory is confined to a single curve [the blue one in Fig. 1(b)]. On the other hand, the FOD droop has two degrees of freedom that can be used to tune  $\sigma$  and  $\zeta$ , which are related to the ST and the overshoot, respectively.

### III. PROPOSED CONTROLLER AND THE MG SSM

#### A. State Space Synthesis of Approximated FO Systems

A few studies discussed the state space synthesis of fractional-order systems [40]. However, to the best of our knowledge, none of these studies gave special treatment for integer order states that require no approximation. A generalized procedure to achieve this target is developed next. Assume the matrix representation of a MIMO system is given as follows:

$$\begin{aligned} [s x_1 \cdots G_\gamma^{-1}(s) x_p \cdots s x_L]^T &= A [x_1 \cdots x_p \cdots x_L]^T + B U \\ Y &= C [x_1 \cdots x_p \cdots x_L]^T + D U \end{aligned} \quad (8)$$

where  $L$  is the number of state variables,  $x_p$  is the state variable with FO dynamics,  $G(s)$  is a transfer function approximation of a FO operator that is not strictly proper,  $U$  is an  $M$ -dimensional input vector, and  $Y$  is an  $O$ -dimensional output vector. The  $p$ th row of the system equation under the approximation given by  $G_\gamma(s)$  can be written as follows:

$$G_\gamma^{-1}(s) x_p = \sum_{i=1}^L a_{p,i} x_i + \sum_{j=1}^M b_{p,j} u_j. \quad (9)$$

Using the observable canonical form to realize (9) in state space format gives the following representation:

$$\dot{\bar{X}}_p = A_\gamma \bar{X}_p + B_\gamma u_n, \quad \bar{x}_p = C_\gamma \bar{X}_p + d u_n \quad (10)$$

where  $\bar{X}_p$  is an  $(N+1) \times 1$  vector, which is the approximation of the fractional dynamic behavior of the variable  $x_p$ , and  $u_n = \sum_{i=1, i \neq p}^L a_{p,i} x_i + \sum_{j=1}^M b_{p,j} u_j$ . The approximation subsystem matrices are given as follows:

$$\begin{aligned} A_\gamma &= \begin{bmatrix} 0 & 0 & \cdots & 0 & -g_0 \\ 1 & 0 & \cdots & 0 & -g_1 \\ \vdots & \vdots & \ddots & \vdots & \vdots \\ 0 & 0 & \cdots & 1 & -g_{N-1} \end{bmatrix}, \quad B_\gamma = \begin{bmatrix} f_0 \\ f_1 \\ \vdots \\ f_{N-1} \end{bmatrix} \\ C_\gamma &= \begin{bmatrix} \mathbf{0} & 1 \end{bmatrix}_{1 \times (N-1)} \end{aligned} \quad (11)$$

where  $g_k$  and  $f_k$  are the coefficients of the rational transfer function given as follows:

$$\frac{G_\gamma}{1 - a_{p,p}G_\gamma} = d + \frac{\sum_{k=0}^{N-1} f_k s^k}{s^N + \sum_{k=0}^{N-1} g_k s^k}. \quad (12)$$

The resulting approximated state space model is given as follows:

$$\begin{aligned} \begin{bmatrix} \dot{x}_1 \cdots \dot{\bar{X}}_p^T \cdots \dot{x}_L \end{bmatrix} &= \bar{A} \begin{bmatrix} x_1 \cdots \bar{X}_p^T \cdots x_L \end{bmatrix}^T + \bar{B}U \\ Y &= \bar{C} \begin{bmatrix} x_1 \cdots \bar{X}_p^T \cdots x_L \end{bmatrix}^T + \bar{D}U \end{aligned} \quad (13)$$

where the approximated system matrix is given in (14), and the approximated input, output, and feed through matrices are given in (15), (16), and (17).

$$\begin{aligned} \bar{A} &= \begin{bmatrix} A_{1:p-1,1:p-1} & [A_{1:p-1,p}C_\gamma] & A_{1:p-1,p+1:L} \\ [B_\gamma A_{p,1:p-1}] & A_\gamma & [B_\gamma A_{p,p+1:L}] \\ A_{p+1:L,1:p-1} & [A_{p+1:L,p}C_\gamma] & A_{p+1:L,p+1:L} \end{bmatrix} \\ &+ d \begin{bmatrix} \tilde{A}_1 & \mathbf{0} & \tilde{A}_2 \\ (p-1) \times (p-1) & (p-1) \times N & (p-1) \times (L-p) \\ \mathbf{0} & \mathbf{0} & \mathbf{0} \\ N \times (p-1) & N \times N & N \times (L-p) \\ \tilde{A}_3 & \mathbf{0} & \tilde{A}_4 \\ (L-p) \times (p-1) & (L-p) \times N & (L-p) \times (L-p) \end{bmatrix} \\ &\times \text{diag} \left( \begin{bmatrix} A_{p,1:p-1} & \mathbf{0} & A_{p,p+1:L} \\ 1 \times N & & \end{bmatrix} \right) \\ \tilde{A}_1 &= [A_{1:p-1,p}] \underbrace{\mathbf{1}}_{1 \times (p-1)}, \tilde{A}_2 = [A_{1:p-1,p}] \underbrace{\mathbf{1}}_{1 \times (L-p)} \\ \tilde{A}_3 &= [A_{p+1:L,p}] \underbrace{\mathbf{1}}_{1 \times (p-1)}, \tilde{A}_4 = [A_{p+1:L,p}] \underbrace{\mathbf{1}}_{1 \times (L-p)} \end{aligned} \quad (14)$$

$$\begin{aligned} \bar{B} &= \begin{bmatrix} \underbrace{I}_{(p-1) \times (p-1)} & \mathbf{0} & \mathbf{0} \\ \mathbf{0} & B_\gamma & \mathbf{0} \\ \mathbf{0} & \mathbf{0} & I \end{bmatrix} B \\ &+ d \begin{bmatrix} \tilde{B}_1 \\ \mathbf{0} \\ \tilde{B}_2 \end{bmatrix} \text{diag} \left( [B_{p,1:M}] \right) \\ \tilde{B}_1 &= [A_{1:p-1,p}] \underbrace{\mathbf{1}}_{1 \times M}, \tilde{B}_2 = [A_{p+1:L,p}] \underbrace{\mathbf{1}}_{1 \times M} \end{aligned} \quad (15)$$

$$\begin{aligned} \bar{C} &= [C_{1:O,1:p-1} \quad [C_{1:O,p}C_\gamma] \quad C_{1:O,p+1:L}] \\ &+ d \left[ \left( [C_{1:O,p}] \times \underbrace{\mathbf{1}}_{1 \times (p-1)} \right) \underbrace{\mathbf{0}}_{O \times N} \left( [C_{1:O,p}] \times \underbrace{\mathbf{1}}_{1 \times (L-p)} \right) \right] \\ &\times \text{diag} \left( \begin{bmatrix} A_{p,1:p-1} & \mathbf{0} & A_{p,p+1:L} \\ 1 \times N & & \end{bmatrix} \right) \end{aligned} \quad (16)$$

$$\bar{D} = D + dC_{1:O,p} \underbrace{\mathbf{1}}_{1 \times M} \text{diag} \left( [B_{p,1:M}] \right). \quad (17)$$

where  $\mathbf{1}$  and  $\mathbf{0}$  are matrices of ones and zeros, respectively, of the indicated dimensions.

In the case of systems with multiple FO states, the developed procedure can be used iteratively. The dimensions of the integer states are not affected by this procedure, which provides a lower dimension of the overall approximated system when compared with other approaches in the literature.

## B. SSM of FOD Droop Controlled IBMG

A detailed and complete SSM is needed to assess the proposed FOD droop controller's stability performance, where the dynamics of the inner controls as well as the *LCL* filters are taken into account. Based on a recent review of MG modeling [41], there are only a few complete and modular MG models in the literature. However, the MG model proposed in [42] has been the base for many models in this category, while the other models have included additional dynamics. Hence, this widely accepted SSM introduced in [42] is adopted in this work and modified to include the new FO controller. The variable naming convention is also carried out from [42] to avoid ambiguity, as most of the model details are skipped here because they are unmodified. The model in [42] is divided into three major submodels: the inverters model, the network model, and the loads model, as shown in Fig. 2(a). These submodels are combined according to the MG structure, i.e., DGs, lines, and load interconnections. The inverter control loop interconnections inside one inverter are illustrated in Fig. 2(b). At each inverter, the *dq* reference frame values of the *LC* filter output voltage ( $v_{odq}$ ) and the *LC* filter output current ( $i_{odq}$ ) are input to the first control stage, the power-sharing controller. Next, this controller dictates the reference values of the voltage controller ( $v_{odq}^*$ ) and also calculates the inverter *dq* reference frame angle ( $\theta$ ). The *LC* filter output current ( $i_{odq}$ ) is also used at the voltage controller in the feedforward path. The innermost controller, the current controller, receives the reference values ( $i_{ldq}^*$ ) from the voltage controller stage and the measured inverter current ( $i_{ldq}$ ) to output the reference value of the inverter voltage ( $v_{idq}^*$ ). The inner controllers, voltage, and current controllers, are traditional *PI* controllers, as adopted in the model in [42]. The modifications in the current work are limited to the power-sharing controller states while maintaining its input–output variables unchanged.

The power controller is dissected into three cascaded stages: the power calculation, the low-pass filters (LPFs), and the droop equations, as shown in Fig. 2(c). The instantaneous active and reactive power,  $\tilde{p}$  and  $\tilde{q}$ , are first calculated from the measured *dq* reference frame values of the *LC* filter output voltage and current, as follows:

$$\tilde{p} = v_{od}i_{od} + v_{oq}i_{oq}, \quad \tilde{q} = v_{oq}i_{od} - v_{od}i_{oq}. \quad (18)$$

Then, a LPF is used to average out these calculated values and provide a separation between the fast inner and the slow outer control loops, producing the slowly varying *P* and *Q* values. Another set of LPFs is also used to filter out the unwanted measurement noise before feeding the filtered values to the

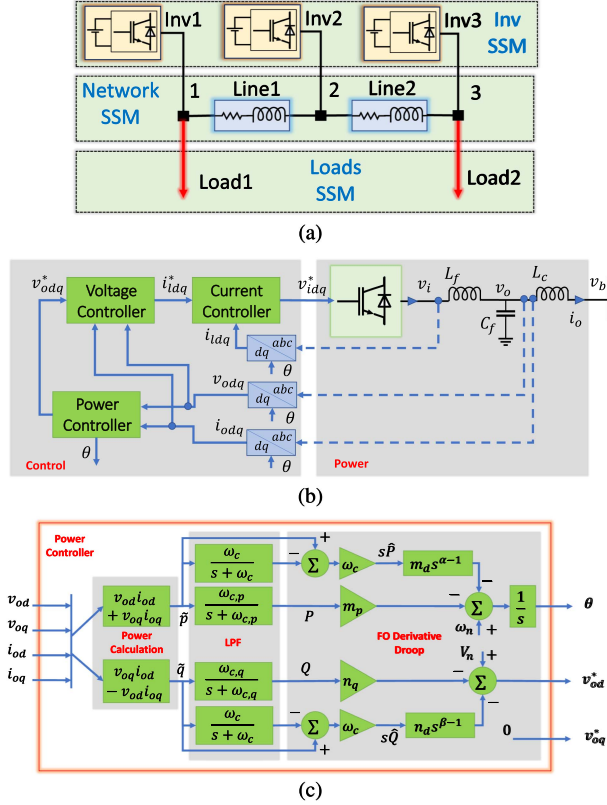


Fig. 2. (a) Benchmark MG configuration and its three major submodels. (b) Inverter internal control loops. (c) Modified power controller with FOD droop in active and reactive paths.

derivative droop controllers, producing  $\hat{P}$  and  $\hat{Q}$ . These four LPFs are described as

$$P = \frac{\omega_{c,p}}{s + \omega_{c,p}} \tilde{p}, Q = \frac{\omega_{c,q}}{s + \omega_{c,q}} \tilde{q}, \hat{P} = \frac{\omega_c}{s + \omega_c} \tilde{p}, \hat{Q} = \frac{\omega_c}{s + \omega_c} \tilde{q}. \quad (19)$$

The structure of the four filters in (19) is identical and can be expressed in the time domain in the form of a differential equation. For example, let us consider the first LPF:

$$\begin{aligned} \frac{d}{dt} P &= -\omega_c P + \omega_c \tilde{p} = -\omega_c P + \omega_c (v_{od} i_{od} + v_{oq} i_{oq}) \\ &= f(P, u) \end{aligned} \quad (20)$$

where  $u = [v_{od}, v_{oq}, i_{od}, i_{oq}]^T$  is an input vector. Using the first-order Taylor series expansion, (20) can be linearized as around an operating point, constant  $(\bar{P}, \bar{u})$ , as follows:

$$\begin{aligned} \frac{d}{dt} P &= \frac{d}{dt} (\bar{P} + \Delta P) = f(P, u) \approx f(\bar{P}, \bar{u}) \\ &+ \left. \frac{\partial f}{\partial P} \right|_{(\bar{P}, \bar{u})} (P - \bar{P}) + \left. \frac{\partial f}{\partial u} \right|_{(\bar{P}, \bar{u})} (u - \bar{u}) \end{aligned} \quad (21)$$

where  $P = \bar{P} + \Delta P$  and  $u = \bar{u} + \Delta u$ . Consequently, the small signal equivalents of (19) are

$$\frac{d}{dt} \Delta P = -\omega_{c,p} \Delta P + \omega_{c,p} (I_{od} \Delta v_{od} + I_{oq} \Delta v_{oq})$$

$$+ V_{od} \Delta i_{od} + V_{oq} \Delta i_{oq})$$

$$\begin{aligned} \frac{d}{dt} \Delta Q &= -\omega_{c,q} \Delta Q + \omega_{c,q} (I_{od} \Delta v_{oq} - I_{oq} \Delta v_{od} \\ &+ V_{oq} \Delta i_{od} - V_{od} \Delta i_{oq}) \end{aligned}$$

$$\begin{aligned} \frac{d}{dt} \Delta \hat{P} &= -\omega_c \Delta \hat{P} + \omega_c (I_{od} \Delta v_{od} + I_{oq} \Delta v_{oq} \\ &+ V_{od} \Delta i_{od} + V_{oq} \Delta i_{oq}) \end{aligned}$$

$$\begin{aligned} \frac{d}{dt} \Delta \hat{Q} &= -\omega_c \Delta \hat{Q} + \omega_c (I_{od} \Delta v_{oq} - I_{oq} \Delta v_{od} \\ &+ V_{oq} \Delta i_{od} - V_{od} \Delta i_{oq}) \end{aligned} \quad (22)$$

where  $\Delta x$  is the small signal value of the variable  $x$ , and  $X$  is the operating point of the same variable.  $\omega_{c,p}$ ,  $\omega_{c,q}$ , and  $\omega_c$  are the cut-off frequencies of the active power droop, reactive power droop, and derivative droop LPFs, respectively.

The droop relations of the proposed FOD droop controller are given as follows:

$$\begin{aligned} \dot{\theta} &= \omega_n - m_p P - m_d P_\alpha \implies \Delta \dot{\theta} = -m_p P - m_d P_\alpha \\ v_{od}^* &= V_n - n_q Q - n_d Q_\beta \implies \Delta v_{od}^* = -n_q Q - n_d Q_\beta \\ v_{oq}^* &= 0 \implies \Delta v_{oq}^* = 0 \end{aligned} \quad (23)$$

where  $\dot{\theta} = \omega$  is the instantaneous frequency of the inverter.  $\omega_n$  and  $V_n$  are the nominal values of the operating frequency and voltage, respectively,  $m_p$  is the active power droop gain, and  $n_q$  is the reactive power droop gain.  $m_d$  and  $n_d$  are the controller gains for the derivatives of the active and reactive powers, respectively. The phase angle is related to the instantaneous frequency as follows:

$$\Delta \dot{\delta} = \int (\omega - \omega_{com}) dt \quad (24)$$

where  $\omega_{com}$  is the frequency of the common  $DQ$  reference frame, which is the same as the first inverter (by choice). The newly introduced FO dynamics variables are defined as

$$\begin{aligned} P_\alpha &= D^\alpha \hat{P} \longrightarrow s^{1-\alpha} P_\alpha = s \hat{P}, \\ Q_\beta &= D^\beta \hat{Q} \longrightarrow s^{1-\beta} Q_\beta = s \hat{Q}. \end{aligned} \quad (25)$$

Although the state space realization of IO systems is not unique, the state space realization of FO systems is even more arbitrary due to the introduced fractional orders. If the recommended procedures outlined in [43] are followed for state space realization of these FOD droop equations, extra FO states will be added. Hence, another realization is proposed to minimize the number of approximated FO states. The Laplace domain small signal matrix representation of the system is given as follows:

$$\begin{aligned} &\begin{bmatrix} s\Delta\delta & s\Delta P & s\Delta\hat{P} & G_\alpha\Delta P_\alpha & s\Delta Q & s\Delta\hat{Q} & G_\beta\Delta Q_\beta \end{bmatrix}^T \\ &= A_p \begin{bmatrix} \Delta\delta & \Delta P & \Delta\hat{P} & \Delta P_\alpha & \Delta Q & \Delta\hat{Q} & \Delta Q_\beta \end{bmatrix}^T \\ &+ B_p \begin{bmatrix} \Delta i_{dq} \\ \Delta v_{odq} \\ \Delta i_{odq} \end{bmatrix} + B_{P\omega_{com}} \begin{bmatrix} \Delta\omega_{com} \end{bmatrix} \end{aligned}$$

$$\begin{bmatrix} \Delta\omega \\ \Delta v_{odq}^* \end{bmatrix} = \begin{bmatrix} C_{P\omega} \\ C_{Pv} \end{bmatrix} \times \begin{bmatrix} \Delta\delta & \Delta P & \Delta\hat{P} & \Delta P_\alpha & \Delta Q & \Delta\hat{Q} & \Delta Q_\beta \end{bmatrix}^T \quad (26)$$

where

$$\begin{aligned} A_P &= \begin{bmatrix} 0 & -m_p & 0 & -m_d & 0 & 0 & 0 \\ 0 & -\omega_{c,p} & 0 & 0 & 0 & 0 & 0 \\ 0 & 0 & -\omega_c & 0 & 0 & 0 & 0 \\ 0 & 0 & -\omega_c & 0 & 0 & 0 & 0 \\ 0 & 0 & 0 & 0 & -\omega_{c,q} & 0 & 0 \\ 0 & 0 & 0 & 0 & 0 & -\omega_c & 0 \\ 0 & 0 & 0 & 0 & 0 & -\omega_c & 0 \end{bmatrix} \\ B_{P\omega com} &= \begin{bmatrix} -1 & 0 & 0 & 0 & 0 & 0 & 0 \end{bmatrix}^T \\ B_P &= \begin{bmatrix} 0 & 0 & 0 & 0 & 0 & 0 & 0 \\ 0 & 0 & \omega_{c,p}I_{od} & \omega_{c,p}I_{oq} & \omega_{c,p}V_{od} & \omega_{c,p}V_{oq} \\ 0 & 0 & \omega_c I_{od} & \omega_c I_{oq} & \omega_c V_{od} & \omega_c V_{oq} \\ 0 & 0 & \omega_c I_{od} & \omega_c I_{oq} & \omega_c V_{od} & \omega_c V_{oq} \\ 0 & 0 & -\omega_{c,q}I_{oq} & \omega_{c,q}I_{od} & \omega_{c,q}V_{oq} & -\omega_{c,q}V_{od} \\ 0 & 0 & -\omega_c I_{oq} & \omega_c I_{od} & \omega_c V_{oq} & -\omega_c V_{od} \\ 0 & 0 & -\omega_c I_{oq} & \omega_c I_{od} & \omega_c V_{oq} & -\omega_c V_{od} \end{bmatrix} \\ C_{P\omega} &= \begin{bmatrix} 0 & -m_p & 0 & -m_d & 0 & 0 & 0 \end{bmatrix}, \\ C_{Pv} &= \begin{bmatrix} 0 & 0 & 0 & 0 & -n_q & 0 & -n_d \\ 0 & 0 & 0 & 0 & 0 & 0 & 0 \end{bmatrix} \end{aligned} \quad (27)$$

$$G_\alpha(s) \approx s^{1-\alpha}, G_\beta(s) \approx s^{1-\beta}. \quad (28)$$

At  $\alpha = \beta \approx 1$ , the poles and zeros of the approximating transfer functions,  $G_\alpha$  and  $G_\beta$ , are almost canceled, and the system in (26) converges to a differential algebraic system that is equivalent to the IO system in [27], [28]. Each inverter has three internal SSMs other than the power controller. These other SSMs are for the voltage controller, the current controller, and the *LCL* filter (kindly refer to [42]). The complete inverter model has 15 pseudostates (only two FO state per inverter). The approximation procedure in Section III-A is performed on the power controller SSM in its matrix form. Hence, the number of states of the approximated inverter model is

$$N_{inv} = 15 + 2 \times N_{app} \quad (29)$$

where  $N_{app}$  is the approximation order for  $P_\alpha$  and  $Q_\beta$  pseudostates, which is assumed to be equal for simplicity. The state space model representation of the approximated  $i$ th inverter is:

$$\begin{aligned} \Delta \dot{\bar{x}}_{invi} &= \bar{A}_{invi} \Delta \bar{x}_{invi} + \bar{B}_{invi} \Delta v_{bDQi} + \bar{B}_{i\omega com} \Delta \omega_{com} \\ \begin{bmatrix} \Delta \omega_i \\ \Delta i_{oDQi} \end{bmatrix} &= \begin{bmatrix} \bar{C}_{invi} \\ \bar{C}_{invc} \end{bmatrix} \Delta \bar{x}_{invi} \end{aligned} \quad (30)$$

where the approximated state vector is given as  $\Delta \bar{x}_{invi} = [\Delta \delta_i, \Delta P_i, \Delta \hat{P}_i, \Delta \bar{P}_{\alpha i}, \Delta Q_i, \Delta \hat{Q}_i, \Delta \bar{Q}_{\beta i}, \Delta \phi_{dq}, \Delta \gamma_{dq}, \Delta i_{ldq}, \Delta v_{odqi}, \Delta i_{odqi}]^T$ . The over-line,  $\bar{X}$ , is used to denote the approximated version of a matrix or a state variable. The details of the approximated inverter matrices and their modified dimensions are given in (31) and (32) shown at the bottom of the next page.

$$\begin{aligned} \bar{B}_{invi} &= \begin{bmatrix} \mathbf{0}_{(N_{inv}-6) \times 2} \\ \underbrace{[B_{LCL2i} T_{Si}^{-1}]}_{6 \times 2} \end{bmatrix}, \bar{B}_{i\omega com} = \begin{bmatrix} \underbrace{[\bar{B}_{P\omega com}]}_{(2N_{app}+3) \times 1} \\ \mathbf{0}_{(N_{inv}-2N_{app}-3) \times 1} \end{bmatrix} \\ \bar{C}_{invi} &= \begin{cases} \begin{bmatrix} \underbrace{[\bar{C}_{P\omega i}]}_{1 \times (2N_{app}+3)} & \mathbf{0}_{1 \times (N_{inv}-2N_{app}-9)} & \underbrace{[\bar{D}_{P\omega i}]}_{1 \times 6} \end{bmatrix} & i = 1 \\ \begin{bmatrix} \mathbf{0}_{1 \times N_{inv}} \end{bmatrix} & & \end{cases} \\ \bar{C}_{invc} &= \begin{bmatrix} T_c & \mathbf{0}_{2 \times (N_{inv}-3)} & T_s \end{bmatrix}. \end{aligned} \quad (31)$$

The complete MG SSM is then synthesized by combining the three major subsystems: the inverter model, the network model, and the loads model. The autonomous MG SSN is given as

$$\begin{bmatrix} \underbrace{[\Delta \dot{\bar{x}}_{INV}]}_{3N_{inv} \times 1} \\ \underbrace{[\Delta i_{lineDQ}]}_{4 \times 1} \\ \underbrace{[\Delta i_{loadDQ}]}_{4 \times 1} \end{bmatrix} = \underbrace{[\bar{A}_{mg}]} \begin{bmatrix} \Delta \bar{x}_{INV} \\ \Delta i_{lineDQ} \\ \Delta i_{loadDQ} \end{bmatrix} \quad (32)$$

where  $\bar{x}_{INV}$  is a state combining the states of all the inverters. The subscript *DQ* refer to the common rotating reference frame (of the first inverter, by choice). The benchmark system provided in [42] has three inverters, two lines, and two loads, as shown in Fig. 2(a). Hence, the entire MG matrix ( $A_{mg}$ ) has  $8 + 3N_{inv}$  rows and columns. For more information about the supporting matrices used to generate  $A_{mg}$ , kindly refer to [27], [28], [42].

#### IV. SIMULATIONS AND RESULTS

In this section, the performance of the IOD and FOD droops is compared from different aspects throughout the following sections. The comparison includes small signal stability and the performance of the tuned controllers under several contingency events, including large load disturbance and reconfiguration through a meshed network. The IOD and FOD droops are applied to the benchmark system in Fig. 2(a), and the default parameters of this system are summarized in the appendix.

##### A. Stability Margin Improvement

In conventional droop, the active power droop gain has been used as an indication of the stability margin. The larger the maximum stable active droop gain, the larger the stability margin

**TABLE II**  
MAXIMUM ACTIVE DROOP GAIN FOR DIFFERENT CONTROLLERS

Droop type	Conventional	IOD	FOD	FOD with tuned LPF
$\alpha$	—	1.0	1.2	1.2
$\beta$	—	1.0	1.4	1.4
$m_d \times 10^{-6}$	0	2	2	2
$n_d \times 10^{-6}$	0	5	5	5
$(w_{c,p}, w_{c,q})$	$(w_c, w_c)$	$(w_c, w_c)$	$(w_c, w_c)$	$(0.5w_c, 3w_c)$
Maximum $m_p \times 10^{-4}$	1.9	4.58	29.8	51.4

of the system [15], [28]. In this section, the same convention is followed to assess the stability margin of various controllers, where the difference between any controller and the next one is a small structural change. Table II compares the maximum achievable  $m_p$  of four droop controllers: conventional droop, IOD droop, FOD droop, and FOD droop with tuned LPF. The conventional droop has the least  $m_{p,\max} = 1.9 \times 10^{-4}$  rad/s/W while the IOD droop improves it to  $m_{p,\max} = 4.58 \times 10^{-4}$  rad/s/W, at integer derivative orders  $\alpha = \beta = 1.0$ . Changing only the fractional orders, the FOD droop achieves a higher  $m_{p,\max} = 29.8 \times 10^{-4}$  rad/s/W at  $\alpha = 1.2$  and  $\beta = 1.4$ . Even further improvement can be obtained using the FOD droop, by tuning the cut-off frequency of its LPF, to get  $m_{p,\max} = 51.4 \times 10^{-4}$  rad/s/W. However, such higher values of  $m_p$  are beyond the operational limits for allowable frequency deviation, which makes the value of  $m_{p,\max}$  no longer suitable for assessing the stability margin. According to the IEEE Std. 1547-2018 [44], the allowable frequency deviation of DGs is within  $\pm 1.2$  Hz; otherwise, the under/over frequency protection relays shall trip. In this work, the values of  $m_p$  are chosen to ensure  $\pm 0.5$  Hz maximum deviation in all studied cases.

### B. Dynamic Performance Improvement

Fig. 3 shows the maximum real part ( $\sigma_{\max}$ ) of the eigenvalues of the  $A_{mg}$  matrix when an exhaustive search is performed in

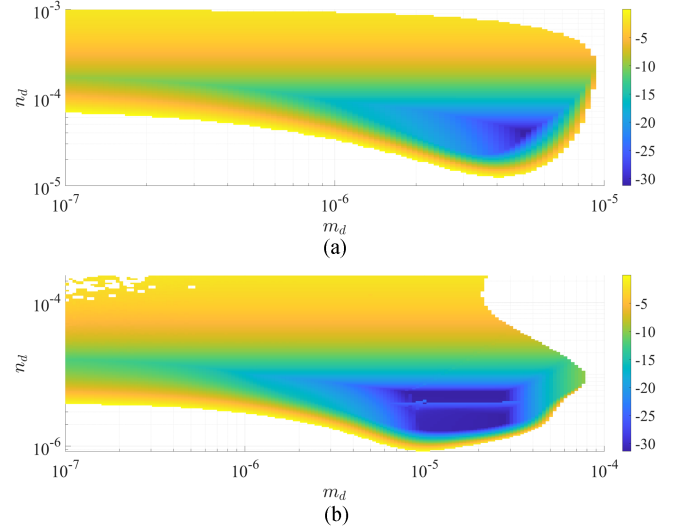


**Fig. 3.** Decay rate ( $\sigma$ ) results of the exhaustive search in the  $m_d$ - $n_d$  plane at (a)  $\alpha = \beta = 1.0$ , and (b)  $\alpha = 0.9$  and  $\beta = 1.5$ . (a) IOD droop. (b) FOD droop.

the  $m_d$ - $n_d$  plane. The exhaustive search approach is common in the design of power system stabilizers, as in [45]. The white spaces indicate unstable combinations of  $m_d$  and  $n_d$ . The wider dark blue area in the FOD droop case shows that the proposed controller can be less sensitive to derivative droop gain variations at certain fractional orders when compared with the IOD droop controller.

One combination of gains for each controller is chosen from Fig. 3 at the same  $\sigma_{\max} \approx 31.0$  (the best achievable value for IOD droop). For the IOD droop  $m_d = 5.1 \times 10^{-6}$  rad/W and  $n_d = 4.1 \times 10^{-5}$  V · s/VAr while for the FOD droop  $m_d = 1.867 \times 10^{-5}$  rad/W,  $\alpha = 0.9$ ,  $n_d = 4.43 \times 10^{-6}$  V · s/VAr, and  $\beta = 1.5$ . The simulation results of these chosen parameters are shown in Fig. 4. It is evident that even at the same  $\sigma_{\max}$ , the FOD

$$\bar{A}_{invi} =$$

$$\left[ \begin{array}{ccc} \underbrace{\begin{bmatrix} \bar{A}_{Pi} \end{bmatrix}}_{(2N_{app}+5) \times (2N_{app}+5)} & \underbrace{\mathbf{0}}_{(2N_{app}+5) \times 2} & \underbrace{\mathbf{0}}_{(2N_{app}+5) \times 2} & \underbrace{\begin{bmatrix} \bar{B}_{Pi} \end{bmatrix}}_{(2N_{app}+5) \times 6} \\ \underbrace{\begin{bmatrix} \bar{B}_{V1i} \bar{C}_{Pvi} \end{bmatrix}}_{2 \times (2N_{app}+5)} & \underbrace{\mathbf{0}}_{2 \times 2} & \underbrace{\mathbf{0}}_{2 \times 2} & \underbrace{\begin{bmatrix} B_{V2i} + B_{V1i} \bar{D}_{Pvi} \end{bmatrix}}_{2 \times 6} \\ \underbrace{\begin{bmatrix} B_{C1i} D_{V1i} \bar{C}_{Pvi} \end{bmatrix}}_{2 \times (2N_{app}+5)} & \underbrace{\begin{bmatrix} B_{C1i} C_{Vi} \end{bmatrix}}_{2 \times 2} & \underbrace{\mathbf{0}}_{2 \times 2} & \underbrace{\begin{bmatrix} B_{C1i} D_{V2i} + B_{C2i} \\ + B_{C1i} D_{V1i} \bar{D}_{Pvi} \end{bmatrix}}_{2 \times 6} \\ \underbrace{\begin{bmatrix} B_{LCL1i} D_{C1i} D_{V1i} \bar{C}_{Pvi} \\ + B_{LCL2i} \begin{bmatrix} T_{vi} & \mathbf{0}_{2N_{app}+4} \end{bmatrix} \\ + B_{LCL3i} \bar{C}_{P\omega_i} \end{bmatrix}}_{6 \times (2N_{app}+5)} & \underbrace{\begin{bmatrix} B_{LCL1i} D_{C1i} C_{Vi} \end{bmatrix}}_{6 \times 2} & \underbrace{\begin{bmatrix} B_{LCL1i} C_{Ci} \end{bmatrix}}_{6 \times 2} & \underbrace{\begin{bmatrix} A_{LCLi} + B_{LCL1i} (D_{C1i} D_{V2i} + D_{C2i}) \\ + B_{LCL3i} \bar{D}_{P\omega_i} + B_{LCL1i} D_{C1i} D_{V1i} \bar{D}_{Pvi} \end{bmatrix}}_{6 \times 6} \end{array} \right] \quad (32)$$



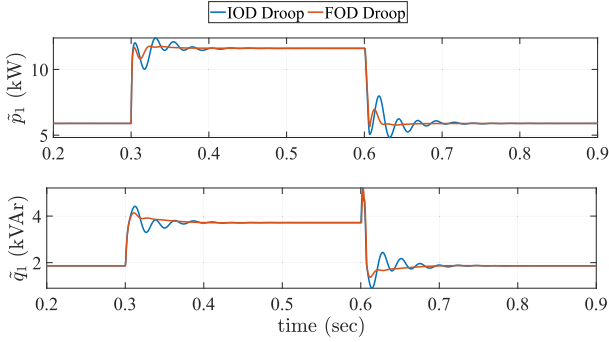


Fig. 4. Instantaneous active and reactive power responses of DG1 using IOD and FOD droop controllers with gains from the exhaustive search under large load disturbance.

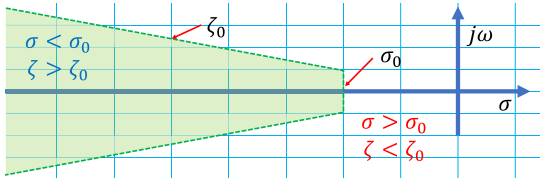


Fig. 5. Desired region of the tracked poles.

droop shows a better dynamic performance when compared to the IOD droop. The improvement factors are the less oscillatory response, the less overshoot, and the faster ST. It is worth noting that the IOD droop point has the least  $\sigma_{\max}$  achievable in the  $m_d$ - $n_d$  plane. Hence, the IOD droop controller requires extra tuning parameters to further improve its performance. This justifies the need for extra LPFs and, more importantly, the FOD droop. However, introducing these extra parameters makes the manual tuning process less efficient. Hence, an optimization-based tuning approach is proposed in the next section.

### C. Optimization Problem Formulation

The proposed objective function aims at tuning the dominant modes of the  $A_{mg}$  to be pushed, as much as possible, within a certain region like the green region in Fig. 5. The indicated region is characterized by two boundaries related to  $\sigma$  (the real part of the pole) and the damping ratio  $\zeta = \cos(\theta_p)$  where  $\theta_p$  is the angle the pole makes with the negative real axis. The first boundary is a vertical line  $\sigma = \sigma_0$  that aims at improving the ST, where the higher the magnitude of  $\sigma$ , the shorter the ST. The second boundary is composed of two slanted lines  $\zeta = \zeta_0$ , and it aims at reducing the overshoot, where higher values of  $\zeta$  lead to lower overshoot. This objective function is inspired by the one proposed in [46] for tuning power system stabilizers. The Problem formulation is defined over multiple loading conditions

$$\min_{(m_d, \alpha, n_d, \beta, \omega_{c,p}, \omega_{c,q})} \text{Max}(J_1, \dots, J_m)$$

$$J_i = a f_1^i + (1 - a) f_2^i, \quad 0 < a < 1$$

TABLE III  
BEST SOLUTIONS OF THE OPTIMIZATION PROBLEM

	$m_d$	$\alpha$	$n_d$	$\beta$	$w_{c,p}$	$w_{c,q}$	fobj
IO	$4.23 \times 10^{-6}$	1.0	$6.79 \times 10^{-5}$	1.0	52.61	39.17	2.56
FO	$2.89 \times 10^{-7}$	1.92	$7.11 \times 10^{-7}$	1.68	125.66	124.95	0.66

$$f_1^i = \sum_{\sigma_j^i > \sigma_0} \frac{|\sigma_j^i - \sigma_0|}{|\sigma_0|}, f_2^i = \sum_{\zeta_j^i < \zeta_0} \frac{|\zeta_j^i - \zeta_0|}{|\zeta_0|} \quad (34)$$

where the superscript  $i = 1, 2, \dots, m$  and  $m$  is the number of loading conditions. The variables of the search vector  $X = [m_d, \alpha, n_d, \beta, \omega_{c,p}, \omega_{c,q}]$  are consistent with Fig. 2(c). The expression  $f_1^i$  penalizes the poles to the right of the vertical line  $\sigma = \sigma_0$  while the expression  $f_2^i$  penalizes the poles having a damping ratio less than  $\zeta_0$ . Together,  $f_1^i$  and  $f_2^i$  achieve the objective of penalizing the poles outside the region described in Fig. 5. However, the approximations of the FO states may have some poles in the penalized region, and these poles don't affect the transient performance. Hence, these FO approximation-related poles must be identified and excluded from the objective function (34), so that the penalty is focused on the ones related to power-sharing dynamics. Based on participation factor analysis (PFA), a pole is identified as a FO pole if all the related states with normalized participation factor greater than 0.1 are fractional ( $P_\alpha, Q_\beta$ ). The tracked poles, the ones included in the calculation of the objective function in (34), are all the poles except the FO ones. The chosen parameters of the optimization problem are  $a = 0.9$ ,  $\sigma_0 = -40$ , and  $\zeta_0 = 0.8$ . The search vector is defined as  $X = [m_d, \alpha, n_d, \beta, \omega_{c,p}, \omega_{c,q}]$ , and the upper and lower bounds are  $Lb = [10^{-8}, 0.1, 10^{-8}, 0.1, 4\pi, 4\pi]$  and  $Ub = [10^{-4}, 1.99, 10^{-4}, 1.99, 40\pi, 40\pi]$ . Without loss of generality, two loading conditions are chosen, which are 33% and 100% loading. The Marine Predator Algorithm (MPA) is used to solve this optimization problem [47], and its results are summarized in Table III. An HPC is used to run the optimization problem with resource allocation of 48 GB of RAM and 25 CPU cores. The average runtime based on 20 independent runs is  $\approx 24$  minutes. Each run has 1000 iterations and 24 search agents. The FOD droop has achieved a lower value of the objective function than the IOD droop. Also, the optimized parameters of the FOD droop show a notable exploitation of the flexibility given by the tunable LPF, while in the case of the IOD droop, the changes in LPF are less.

### D. Comparison With Other Controllers

The locations of the dominant modes of the  $A_{mg}$  matrix are shown in Fig. 6 at the exhaustive search parameters and the tuned parameters. For the IOD droop, the dominant oscillating modes are related to  $\delta_2$  and  $\delta_3$  (from PFA) are pushed further to the left with a new real part ( $\approx -40$ ). However, the damping ratio of these poles is slightly improved for the first pole ( $-40.0 \pm 292.8i$ ) from  $\zeta = 0.12$  to  $\zeta = 0.135$  and reduced for the second pole ( $-40.0 \pm 91.1i$ ) from  $\zeta = 0.453$  to  $\zeta = 0.402$ .

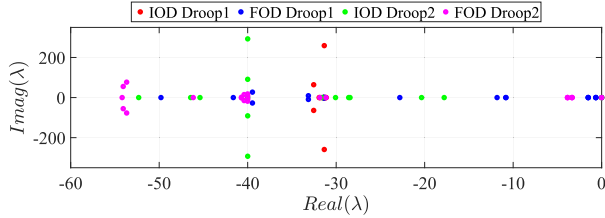


Fig. 6. Poles of the IOD and FOD droop before and after the optimization procedure.

Unfortunately, both these poles are outside the required range for  $\zeta$  even after the optimization. For the FOD droop, the tracked oscillating dominant modes are pushed beyond  $\sigma = -40$  with a  $\zeta > 0.911$  for the poles clustered around  $\sigma = -40$  and  $\zeta > 0.57$  for the poles with real part  $\sigma \approx -54$ . Although some of the tracked poles of the optimized FOD droop are outside the required region for  $\zeta$ , the damping ratios of the dominant optimized IOD droop are worse.

Fig. 7 compares the dynamic performance of the optimized IOD droop, FOD droop, conventional droop, VSG, and VOC controllers under large load disturbance. The tuning procedure of VOC controller parameters is followed from [48], where the parameter  $C$ , the capacitance of the Van der-pol oscillator, is chosen to achieve the fastest rise time without exceeding the maximum recommended third-to-first harmonic ratio of 2%. VSG parameters are  $J = 1.6$  and  $D = 1.59 \times 10^4$ . The conventional droop is included at  $m_p = 0.8 \times 10^{-4}$  rad/s/W, where its maximum stable active droop gain is  $1.9 \times 10^{-4}$  rad/s/W for this benchmark MG. The frequency waveform is included only for DG1, as the other DGs show almost identical frequency dynamics. At  $t = 0.3$  seconds, loads 1 and 2 are increased from 40% to 80%, then at  $t = 0.6$  seconds, the loads are reduced again to 40%. The optimized FOD droop shows a less oscillatory response with a faster ST than the optimized IOD droop. A steady state ripple is observed in VOC, while a slower ST with a higher overshoot is observed in VSG and conventional droop control. Tables IV and V summarize the time domain performance metrics of Fig. 7. The metrics are the ST in seconds, the percentage overshoot (OS%), the percentage undershoot (US%), and the root mean squared error (RMSE). The boldface cells in Tables IV and V denote the best value among the compared controllers. Due to the steady-state ripple of VOC and to accurately calculate the entries of Tables IV and V, the active and reactive power are time averaged over one cycle, as indicated in [48]. The superiority of the FOD droop is evident in most of the cells. VSG control only wins at OS% of  $\tilde{q}_3$ , while VOC prevails at all US% of  $\tilde{q}_i$  in the load-out event due to its different reactive power-sharing steady-state characteristics. IOD droop only ties with FOD droop at OS% of  $\tilde{q}_1$  at the load-in event. The overshoot is less than 1% for  $\tilde{p}_1$  and  $\tilde{p}_2$  in the case of the FOD droop, while it is between 4.2% and 39% for the other controllers. Also, at the same responses, the  $ST$  is between 3 ms and 14 ms for the FOD droop, while it is between 10 ms and 234 ms for the other controllers. The RMSE values are the best in the case of FOD in the load-in event and most of the load-out event, while the VOC

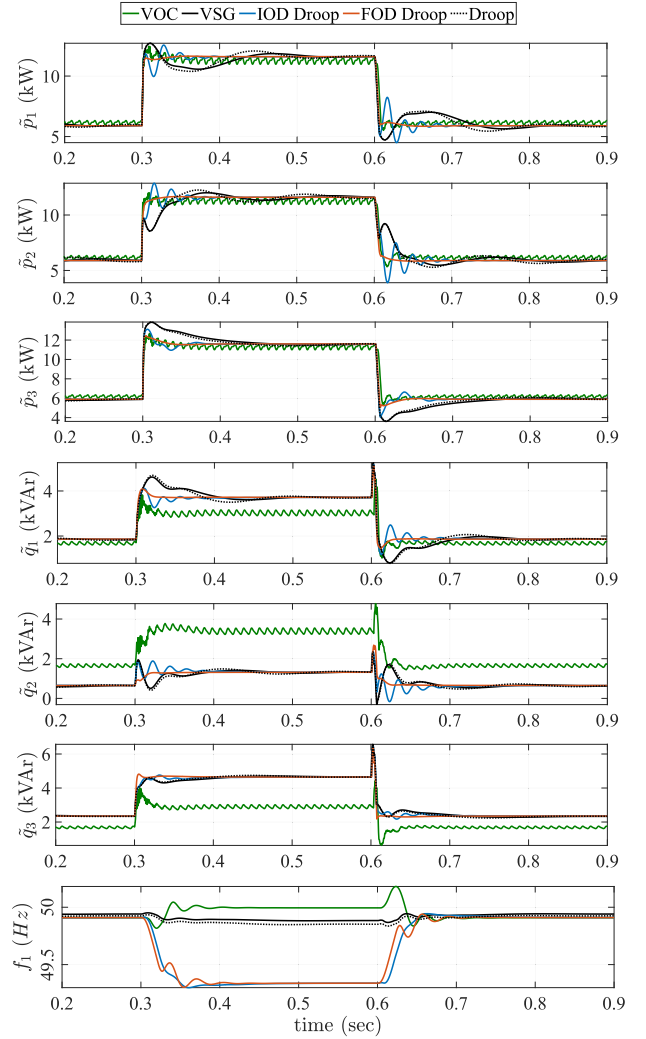


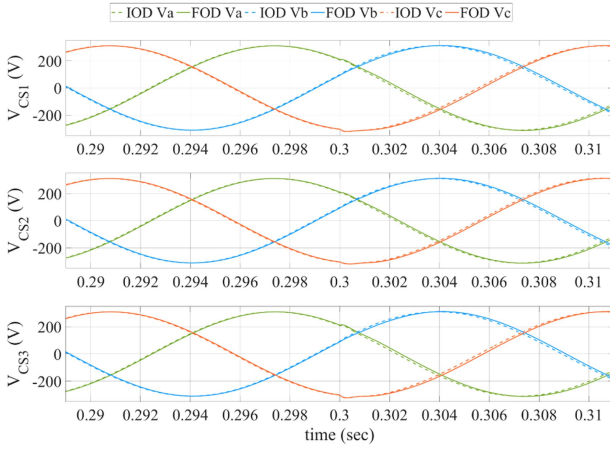
Fig. 7. Instantaneous active and reactive power responses of the DG units and the frequency waveform measured at DG1, using the tuned gains of the IOD droop, FOD droop, VSG control, VOC controller, and conventional droop controller under large load disturbance.

TABLE IV  
LARGE LOAD-IN TIME RESPONSE PERFORMANCE COMPARISON

		IOD	FOD	VSG	VOC	Droop
$\tilde{p}_1$	ST	0.050707	<b>0.00291</b>	0.120576	0.041125	0.16312
	OS%	16.81172	<b>0.756532</b>	19.04285	13.17911	18.20
	US%	0	0	0	0	0
	RMSE	371.2394	<b>229.2345</b>	556.7874	594.6161	622.036
$\tilde{p}_2$	ST	0.05095	<b>0.010971</b>	0.101227	0.01003	0.23297
	OS%	22.16703	<b>0.955082</b>	7.047226	4.227422	13.1444
	US%	0	0	0	0	0
	RMSE	455.5125	<b>283.7654</b>	790.9197	595.0232	790.8795
$\tilde{p}_3$	ST	0.044401	<b>0.022461</b>	0.117715	0.043881	0.09118
	OS%	26.4273	<b>14.56103</b>	39.55384	16.52751	39.2343
	US%	0	0	0	0	0
	RMSE	333.4238	<b>244.1697</b>	790.288	596.6884	726.7504
$\tilde{q}_1$	ST	0.049758	<b>0.018908</b>	0.148947	0.027999	0.15203
	OS%	<b>21.38826</b>	<b>20.0489</b>	48.82016	28.79156	52.2339
	US%	0	0	0	0	0
	RMSE	153.6784	<b>131.6326</b>	298.9999	174.5863	319.653
$\tilde{q}_2$	ST	0.130846	<b>0.040962</b>	0.246662	0.075838	0.27296
	OS%	84.44765	<b>0</b>	89.16741	11.96111	88.25254
	US%	0	0	21.20918	0	33.20246
	RMSE	127.6019	<b>83.03271</b>	199.721	276.5153	231.768
$\tilde{q}_3$	ST	0.066439	<b>0.00738</b>	0.090072	0.060241	0.0714
	OS%	5.033155	<b>7.422143</b>	<b>2.12859</b>	53.06289	4.291356
	US%	0	0	0	0	0
	RMSE	178.5676	<b>145.6977</b>	214.3485	179.3364	204.809

**TABLE V**  
LARGE LOAD-OUT TIME RESPONSE PERFORMANCE COMPARISON

		IOD	FOD	VSG	VOC	Droop
$\tilde{p}_1$	ST	0.062554	<b>0.006157</b>	0.12023	0.035886	0.16258
	OS%	24.45207	<b>0.774476</b>	20.02956	6.331114	18.8116
	US%	5.34E-05	<b>0</b>	0.003037	0.001066	0
	RMSE	674.2611	<b>553.5335</b>	742.8427	890.5279	791.886
$\tilde{p}_2$	ST	0.072306	<b>0.014217</b>	0.161193	0.02657	0.23493
	OS%	34.97014	<b>0.865085</b>	7.673976	10.21578	12.9699
	US%	0	<b>0</b>	0	0.001208	0.01720
	RMSE	788.6221	<b>604.6691</b>	945.3494	907.8225	939.218
$\tilde{p}_3$	ST	0.045041	<b>0.02513</b>	0.121165	0.035794	0.092999
	OS%	32.99612	14.58705	40.94521	<b>6.543194</b>	38.9095
	US%	2.49E-06	<b>0</b>	0.002134	0.001039	0
	RMSE	572.3125	<b>538.6669</b>	880.7766	884.1386	836.794
$\tilde{q}_1$	ST	0.067869	<b>0.022091</b>	0.151947	0.040623	0.15345
	OS%	37.12742	<b>21.772</b>	57.88393	27.76082	57.0773
	US%	78.85749	75.67007	83.66482	<b>38.80323</b>	82.44311
	RMSE	418.5828	383.2699	497.3004	<b>337.3228</b>	506.5747
$\tilde{q}_2$	ST	0.13303	<b>0.043567</b>	0.246268	0.073644	0.272495
	OS%	121.0331	<b>0</b>	127.942	6.689968	138.2489
	US%	151.96	205.0128	143.1179	<b>29.50454</b>	148.7527
	RMSE	<b>242.694</b>	255.0919	301.5049	482.6712	315.8129
$\tilde{q}_3$	ST	0.068251	<b>0.00774</b>	0.093419	0.043304	0.074212
	OS%	7.770879	7.463774	<b>2.219943</b>	58.5319	4.25948
	US%	77.96506	74.39007	82.90685	<b>42.9979</b>	83.275
	RMSE	495.3809	461.5886	528.2994	<b>318.1391</b>	526.823



**Fig. 8.** Control signals in the  $abc$  reference frame for inverters 1, 2, and 3 at the load-in instant.

has the best RMSE values only in the load-out event for  $\tilde{q}_1$  and  $\tilde{q}_3$ . The conventional droop controller shows similar dynamic behavior to the VSG controller in this study. Considering the frequency waveform in Fig. 7, the IOD and FOD droops have identical steady-state characteristics, while VSG and VOC are dissimilar due to differences in equivalent droop gains. VOC shows frequency oscillations and overshoots above 50 Hz, more evidently during the load-out event. VSG has the least frequency variations. Between IOD and FOD droop controllers, the frequency waveform for FOD droop shows some oscillations, but it is within the overshoot and ST of the IOD droop.

Fig. 8 illustrates a snapshot, at the instant of the load-in event, for the control signals in the  $abc$  reference frame that drives the inverters. These control signals are synthesized from a  $dq$ - $abc$  transformation block whose inputs are the phase angle generated from the active power droop controller and the current controller output ( $v_{dq}$ ). A combination of phase and voltage amplitude changes are observed in the case of IOD and FOD droop but with different levels. During real implementation, constraints on the

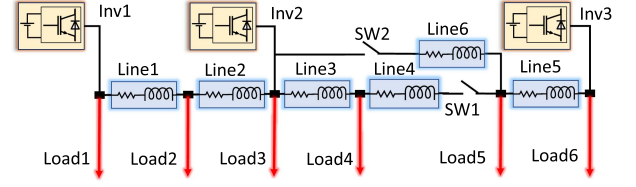


**Fig. 9.** MG diagram for the reconfiguration and meshed network case study.

phase angle or the voltage magnitude are not required for the safe operation of the inverter. The dc link voltage already limits the inverter voltage amplitude and is predetermined during the design phase. However, the inverter current must be limited to protect the power electronic switches in case of faults or current surges.

The proposed controller, FOD droop, can be extended to unbalanced systems based on the idea of positive and negative sequence droops [49]. The sequence theory of unbalanced systems suggests that the superposition principle is applicable to describe unbalanced systems in terms of positive and negative sequence components. Hence, in the unbalanced case, positive and negative sequence droop controllers can be tuned separately, similar to the balanced case. So, the driving equation and formulation of the problem would remain the same in both sequences.

### E. Case Study of a Meshed Network

In this section, the proposed controller is tested under a reconfiguration scenario. The MG under study is shown in Fig. 9, and it is adopted from [50]. Initially, switch 1 is closed, and switch 2 is open. At 0.3 s, switch 2 is closed, and then at 0.6 s, switch 1 is opened. Hence, the MG transitions from radial configuration to mesh configuration to radial again. Based on the study in [50], it is known that the mesh network configuration reduces the stability margin of the system. The derivative droop parameters are as mentioned in Table III, and the active droop gain is  $m_p = 5.7 \times 10^{-4}$  rad/s/W. Fig. 10 shows the active and reactive power responses of each DG at the aforementioned transitions. The first transition, from radial to meshed, shows a larger disturbance in the active and reactive power of the DGs than the second one, from meshed to radial. This is due to the sudden creation of a lower impedance path between buses 3 and 5. It is evident that the FOD droop has a less oscillatory response and a lower overshoot and undershoot at these transition instances when compared with the IOD droop. For instance, the maximum and minimum values of  $\tilde{p}_3$  at the first transition are 17.3 and 11.11 kW for the IOD droop and 15.95 and 14.04 kW for the FOD droop. Also, the maximum and minimum values of  $\tilde{q}_3$  at the first transition are 6.04 and 3.12 kVar for the IOD droop and 5.43 and 3.58 kVar for the FOD droop. The dynamic performance of the conventional droop is slower, with higher overshoot in most cases compared to IOD and FOD droop. The frequency waveform has less overshoot and undershoot in the case of FOD droop compared to the IOD droop. The conventional droop shows almost constant frequency dynamics at higher operating frequency due to the smaller active droop gain ( $m_p = 0.8^{-4}$  rad/s/W).

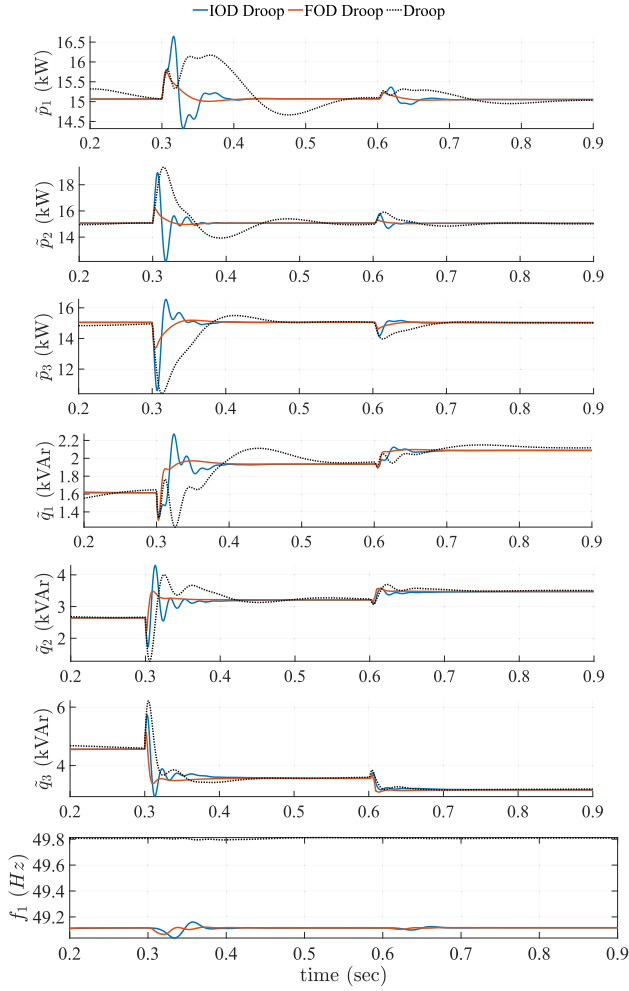


Fig. 10. Instantaneous active and reactive power responses of the DG units and the frequency waveform measured at DG1, using the tuned gains of the IOD droop and FOD droop controllers and the conventional droop controller at the event of two-step reconfiguration.

## V. SENSITIVITY ANALYSIS AND PARAMETER UNCERTAINTY

This section studies the sensitivity of the proposed controller and its performance under various disturbances and parameter uncertainty both in small signal stability analysis and time domain simulations. The studied controller parameters are the derivative droop gains,  $m_d$  and  $n_d$ , and the derivative droop orders,  $\alpha$  and  $\beta$ . The studied model parameters are the impedance of lines one and two. The model parameters of the inverter  $LC$  filter ( $L_f$  and  $C_f$ ) and  $L_c$  and  $R_c$  of the coupling line are ignored due to their insignificant effect on the power-sharing dynamics within practical uncertainty levels. Also, it is found that changing the loading between 10% and 100% does not affect the modes in the dominant eigenvalues region.

In Figs. 11 and 12, the eigenvalues trajectories are plotted in shades of cyan, where the shades go from darker to lighter as the sweeping parameter increases. Also, the red eigenvalues are the ones for the default system parameters (from the Appendix) using the tuned FOD droop controller parameters (from Table II). Based on PFA, the dominant modes (closest to

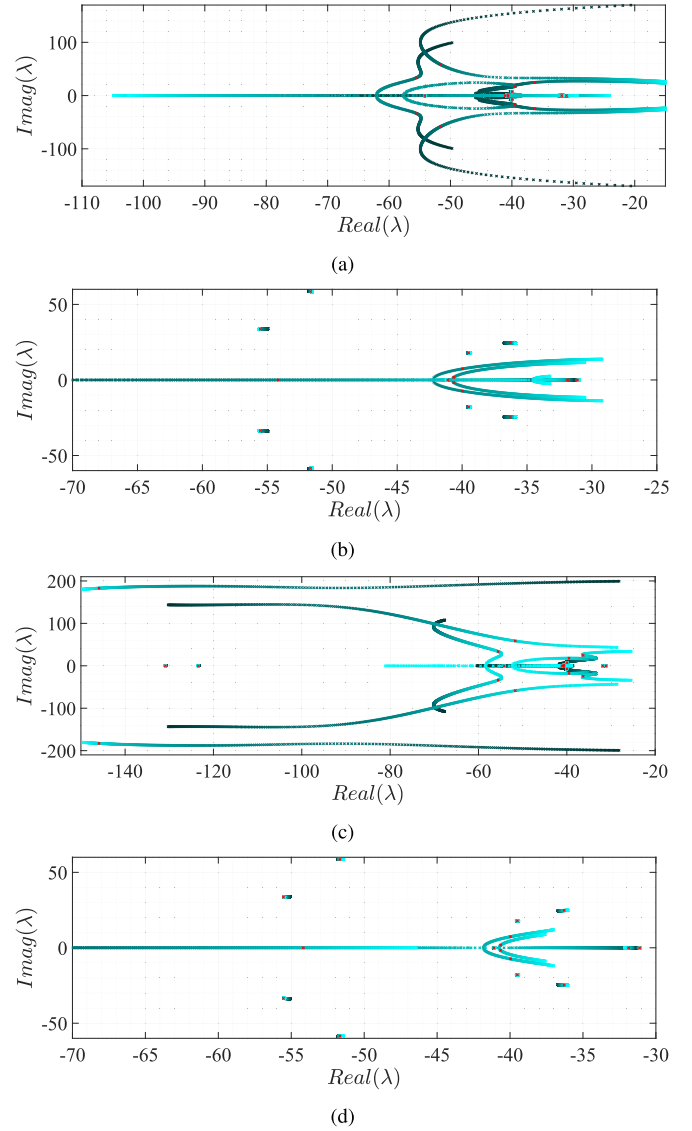


Fig. 11. Dominant modes of the complete SSM at different FOD droop parameters. (a)  $m_d$ , (b)  $n_d$ , (c)  $\alpha$ , and (d)  $\beta$ .

$j\omega$  axis) are associated with the states of active power, reactive power,  $\delta_2$ , and  $\delta_3$ , which are the ones affecting the power-sharing dynamics. To facilitate the description of the trajectories, symbols are assigned to certain red eigenvalues in the dominant region as follows:  $\lambda_1 = -36.2 \pm 24.8i$ ,  $\lambda_2 = -39.4 \pm 17.9i$ ,  $\lambda_3 = -39.9 \pm 7.36i$ ,  $\lambda_4 = -40.6 \pm 1.7i$ ,  $\lambda_5 = -51.66 \pm 58.56i$ ,  $\lambda_6 = -55.5 \pm 33.5i$ , and  $\lambda_7 = -145.89 \pm 182.9i$ .

The eigenvalue trajectories of the MG under study for variations of the proposed controller parameters are investigated in Fig. 11. In Fig. 11(a),  $m_d$  varies between  $0.5 \times 10^{-7}$  and  $8 \times 10^{-7}$ , from dark to light shades of cyan, where the tuned value of  $m_d = 2.89 \times 10^{-7}$  is plotted in red. At  $m_d = 0.5 \times 10^{-7}$ ,  $\lambda_5$  starts at  $-20.6 \pm 169.85i$  (associated with  $\delta_2$  based on PF) has the biggest real part and lowest damping ratio, which causes more overshoot and more ST. As  $m_d$  increases,  $\lambda_5$  and  $\lambda_6$  decrease in real part and increase in damping ratio. The opposite happens in  $\lambda_1$  and  $\lambda_2$ , until  $m_d = 2.89 \times 10^{-7}$ , when

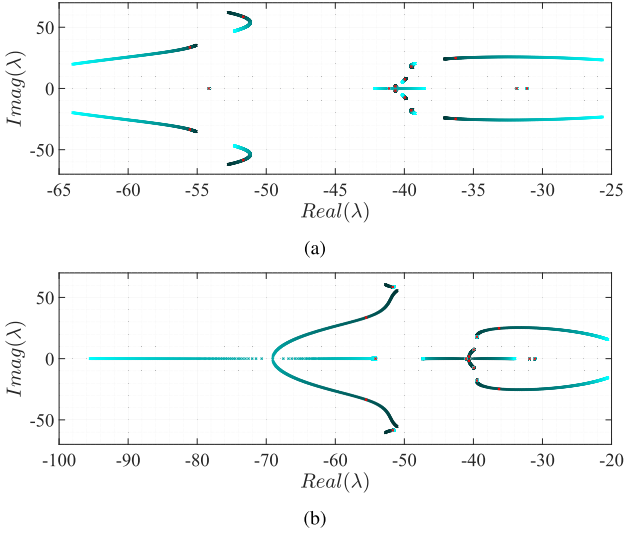


Fig. 12. Dominant modes of the complete SSM at different line impedance values. (a) Line 1, (b) Line 2.

$\lambda_2$  changes direction to decreasing the real part. However, any further increase in  $m_d$  increases the real part of  $\lambda_1$  and  $\lambda_5$  as they move toward the unstable region. Fig. 11(b) shows the eigenvalue trajectories when varying  $n_d$  from  $10^{-7}$  to  $15 \times 10^{-7}$ . Poles  $\lambda_3$  and  $\lambda_4$  are more sensitive to changes in  $n_d$ . They start on the real axis, then move towards the right as complex conjugate pairs when  $n_d$  increases, increasing the real part and reducing the damping ratio. However, based on PFA, at  $n_d = 10^{-7}$ ,  $\lambda_3$  and  $\lambda_4$  are not associated with physical states like  $P_s$ ,  $Q_s$ , or  $\delta_s$ , but, at  $n_d = 10^{-7}$  there is a pole at  $-25.58 \pm 395.7i$  (coming from the less dominant region) that is highly associated with  $\delta_2$  (high PF). Fig. 11(c) illustrates the eigenvalues trajectory when varying the active power FOD droop order  $\alpha$  between 1.6 and 1.99. At  $\alpha = 1.6$ ,  $\lambda_7$  is mainly linked to  $\delta_2$  (based on PFA) and attains a value of  $-28.16 \pm 199.3i$ , causing overshoot and higher frequency oscillations in the power-sharing dynamics. As  $\alpha$  increases,  $\lambda_7$  moves towards the left while  $\lambda_1$ ,  $\lambda_2$ ,  $\lambda_5$ , and  $\lambda_6$  move toward the right. At  $\alpha = 1.9$ ,  $\lambda_2$  and  $\lambda_6$  move to the left with increasing  $\alpha$ , improving the damping ratio but decreasing the real part. Fig. 11(d) shows the eigenvalues movement when changing the reactive power derivative droop order  $\beta$  between 1.4 and 1.8. The behavior is qualitatively similar to the pole movement with changing  $n_d$ .

Next, the eigenvalues trajectories of the proposed controller having uncertainty in MG parameters are shown in Fig. 12. Considering line 1 impedance, Fig. 12(a) shows the eigenvalues trajectories when the impedance is varied between 0.1 and 5 times its nominal value.  $\lambda_1$  and  $\lambda_6$  are more sensitive to the changes in line 1 impedance. The normalized PF of  $\lambda_1$  is 0.32 for  $\delta_3$  and  $\lambda_6$  is 0.209 for  $P_1$  at the maximum impedance ( $5\times$ ), and these PF values are the same or even less for the least impedance ( $0.1\times$ ). Hence, the transient performance differences of power-sharing dynamics are not expected to be significant. In the case of line 2 impedance variations, Fig. 11(c) shows the eigenvalues trajectories when the impedance of line 2 is varied between 0.1 and 5 times its nominal value.  $\lambda_1$ ,  $\lambda_4$ , and  $\lambda_6$  have

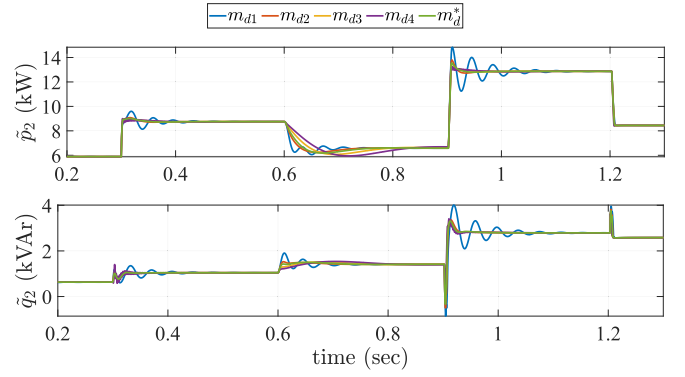


Fig. 13. Active and reactive power responses of DG2 for different  $m_d$ .

longer trajectories, which means they are more sensitive to line 2 impedance variation. The normalized PF values at  $5\times$  the impedance is 1.0 for  $\lambda_6$  and  $P_3$  state and 0.83 for  $\lambda_1$  and  $\delta_3$  state. However, at  $0.1\times$  the impedance, these PF values are 0.16 for  $P_3$  state and less than 0.1 for  $\delta_3$  state, which implies differences in transient performance.

Next, a sensitivity analysis of the proposed controller and its performance under MG parameter uncertainty is performed in simulations for the MG in Fig. 2(a). In time domain simulations, a series of events are executed that provide different levels (large and small) and types of disturbances. First, a load disturbance is made at load one, where its  $P$  and  $Q$  are doubled from 40% to 80% (E1 at  $t = 0.3$  s), and load two is unchanged. After that, the active droop gain of inverter three is halved to have a proportional power sharing where inverter three contributes more than inverters one and two (E2 at  $t = 0.6$  s). After that, inverter three is disconnected, leading to an equal active power sharing between inverters one and two (E3 at  $t = 0.9$  s). The last event is line one disconnection (E4 at  $t = 1.2$  s).

Fig. 13 shows the active and reactive power responses of DG2 under different  $m_d$  values, which is equal to  $0.5 \times 10^{-7}$ ,  $2 \times 10^{-7}$ ,  $5 \times 10^{-7}$ , and  $8 \times 10^{-7}$  for  $m_{d1}$  through  $m_{d4}$ , respectively, where  $m_d^*$  is the tuned value from Table II ( $m_{d2} < m_d^* < m_{d3}$ ). For the active power,  $m_{d1}$  has the highest overshoot and observable oscillation, while  $m_{d4}$  has higher frequency oscillations of smaller magnitude in E1 and E3. In E2, overshoot and ST increases with increasing  $m_d$ , while the opposite happens in E3. For the reactive power, oscillation and overshoot behavior of  $m_{d1}$  and  $m_{d4}$  are the same as in the active power. The performance of  $m_{d2}$ ,  $m_{d3}$ , and  $m_d^*$  is almost the same for events 1, 3, and 4; however, their rise time is increased by increasing  $m_d$  in E2. Fig. 14 shows the responses of DG2 under different  $n_d$  values, which are equal to  $1 \times 10^{-7}$ ,  $4 \times 10^{-7}$ ,  $10 \times 10^{-7}$ , and  $15 \times 10^{-7}$  for  $n_{d1}$  through  $n_{d4}$ , respectively, while  $n_d^*$  is the tuned value from Table II ( $n_{d2} < n_d^* < n_{d3}$ ). For active power, case  $n_{d1}$  is the only case that is distinguishable from the others, and it has overshoot and oscillations in E1 and E3. For reactive power, the overshoot decreases with increasing  $n_d$  in E3. Case  $n_d^*$  has the lowest overshoot and undershoot in E1. Fig. 15 shows the responses of DG2 under different  $\alpha$  values, which are equal to 1.6, 1.7, 1.8, and 1.9 for  $\alpha_1$  through  $\alpha_4$ , respectively, while

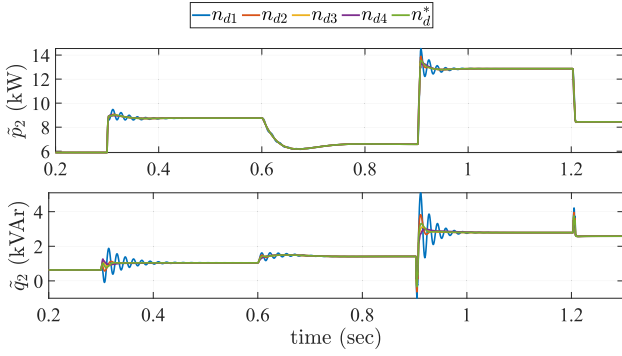


Fig. 14. Active and reactive power responses of DG2 for different  $n_d$ .

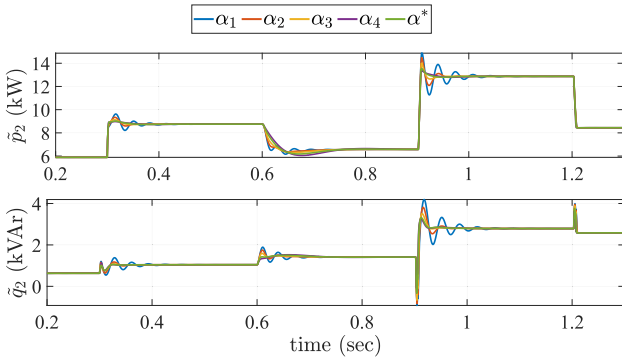


Fig. 15. Active and reactive power responses of DG2 for different  $\alpha$ .

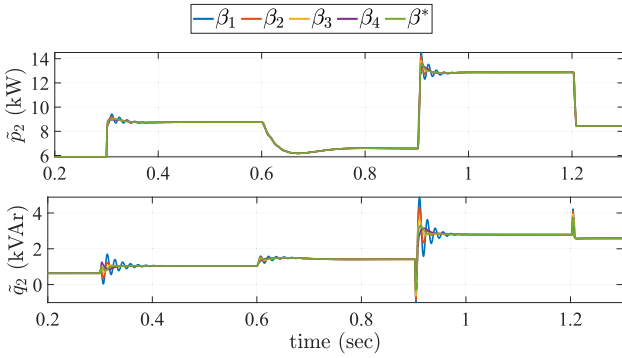


Fig. 16. Active and reactive power responses of DG2 for different  $\beta$ .

$\alpha^*$  is the tuned value from Table II ( $\alpha_3 < \alpha^* < \alpha_4$ ). The case  $\alpha_1$  has the highest overshoot and oscillations in both active and reactive power responses. For the active power, the overshoot decreases with increasing  $\alpha$  in E1 and E3; however, the ST is the best in the case of  $\alpha^*$ . For the reactive power, the overshoot is reduced by increasing  $\alpha$  in E2 and E3. Fig. 16 shows the responses of DG2 under different  $\beta$  values, which are equal to 1.6, 1.7, 1.8, and 1.9 for  $\beta_1$  through  $\beta_4$ , respectively, while  $\beta^*$  is the tuned value from Table II ( $\beta_3 < \beta^* < \beta_4$ ). Oscillations and high overshoot are observed in the case of  $\beta_1$  in active and reactive power responses. For the active power, overshoot is decreased with increasing  $\beta$  in E1 and E3. E2 and E4 are not affected by changing  $\beta$ . For the reactive power,  $\beta^*$  strikes a balance between overshoot, undershoot, and transient time. In

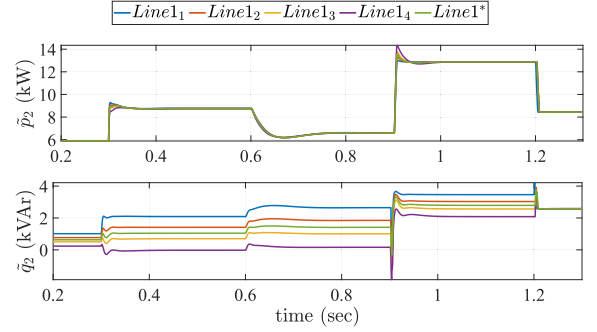


Fig. 17. Active and reactive power responses of DG2 for different line 1 impedance.

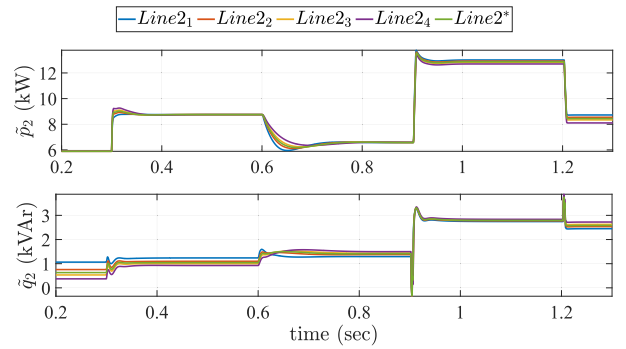


Fig. 18. Active and reactive power responses of DG2 for different line 2 impedance.

summary, it is observed that the steady-state values of the active and reactive power are independent of the FOD droop controller parameters. Also, variation of  $n_d$  and  $\beta$  has less effect on the active power transient than the effect of varying  $m_d$  and  $\alpha$  on the reactive power transients. Also, the tuned values summarized in Table II strike a balance between overshoot and response speed.

Fig. 17 shows the effect of varying line 1 impedance on the transient performance of power-sharing under the proposed controller. The nominal impedance of line 1 ( $Line1^*$ ) is multiplied by factors of  $0.2\times$ ,  $0.7\times$ ,  $1.3\times$ , and  $2.0\times$  in cases  $Line1_1$  through  $Line1_4$ , respectively. For active power, the responses are indistinguishable in E2 and E4. However, in E1, the overshoot decreases as the line impedance increases, while in E3, it is the opposite. Transient time is the same for all cases in E1, while it increases by increasing the line impedance in E3. For reactive power, the steady-state values differ as the line impedance changes, which slightly affects the transient behavior. Overall, changes in the dynamic response are small under the studied uncertainty in line 1 impedance. Fig. 18 shows the effect of varying line 2 impedance on the transient performance of power-sharing under the proposed controller. The nominal impedance of line 2 ( $Line2^*$ ) is multiplied by factors of  $0.2\times$ ,  $0.7\times$ ,  $1.3\times$ , and  $2.0\times$  in cases  $Line2_1$  through  $Line2_4$ , respectively. For the active power, steady-state values after E3 and E4 differ when the line impedance changes. Transient performance in E3 is indistinguishable. The overshoot in event one is increased by increasing the impedance. In E2, the overshoot is higher for

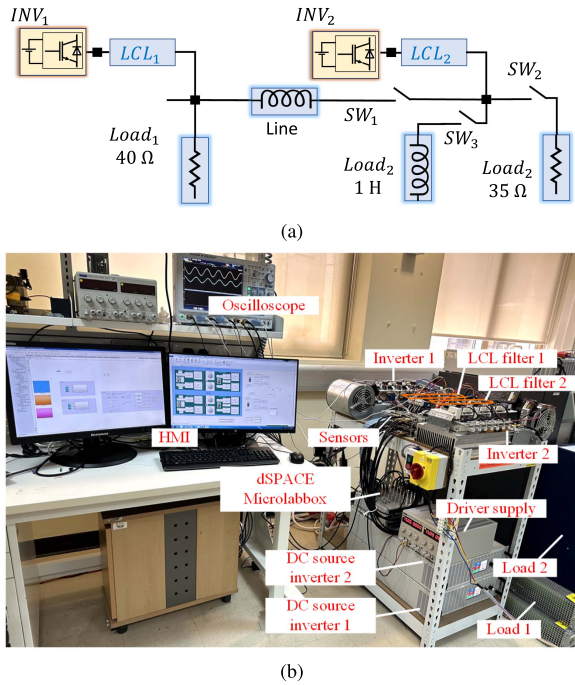


Fig. 19. (a) MG diagram for the experimental setup. (b) Experimental setup of two parallel VSC MG.

lower impedance values of line 2. For the reactive power, the steady-state values are different for different line 2 impedances, which affects the transient behavior. For example, a higher overshoot is observed for the lower values of line 2 impedance in event 2. The variation of dynamics in E3 is negligible. Overall, the proposed controller provides similar dynamic performance under the studied uncertainty ranges of line 2 impedance.

## VI. EXPERIMENTAL VALIDATION

A laboratory scale MG has been developed to validate the performance of the proposed FOD droop controller. The block diagram of the experimental test setup is shown in Fig. 19(a). The experimental setup shown in Fig. 19(b) is constructed with two VSCs working in parallel to form an islanded MG. Two-level three-phase three-leg inverters rated for 20 kVA are used in the system. Both the inverters are connected to the PCC through an LCL filter and a switch ( $SW_1$ ). On the dc side, each converter is powered by a dc power supply rated for 10 kW. dSPACE Microlabbox is used as the controller for both the inverters. Execution time for the controller is optimized by separating the controller's time step, PWM time step, and data sampling time steps. The base time step for computation is set at  $50\mu s$ , where the actual execution time of the control algorithm does not exceed  $36\mu s$ , leaving a safe  $\approx 28\%$  margin. PWM and ADC sampling blocks are triggered from independent timers, which are triggered at 10 and 100 kHz, respectively. The inverters are connected to a switchable load bank consisting of a 3 kW resistive load bank connected in parallel with a 3kVAR inductive load bank. An additional line inductance is connected between two inverters at PCC to emulate the transmission line impedance

characteristics. Detailed parameters of the experimental setup are provided in the appendix.

To test the performance characteristics of different droop controllers, a three-step procedure is followed. First, individual inverters are powered up with their base loads when  $SW_1$  is OFF. Hereafter, inverter 1 is termed as the running inverter, while inverter 2 is called the oncoming machine. In the second step, the droop control is activated, and a synchronization procedure is conducted, as described next. Due to the differences in load and power variations, there will be differences in terminal frequency at the PCC, and due to this, the voltage waveform of the incoming machine traverses across the voltage of the running machine on the oscilloscope. While monitoring the voltage waveforms and by slightly adjusting the load on the oncoming inverter,  $SW_1$  is closed when voltage waveforms are aligned on the oscilloscope (phase angle matching). After connection, the droop controller, along with the tuned inner voltage control and current controller ensures steady operation by redistributing load according to the droop coefficients of the individual inverters. In the last step, controller performance is evaluated by creating a load disturbance on the parallel inverter system using the resistive load bank 2 through  $SW_2$ . The instantaneous power output of each inverter is internally calculated in the controller and sent to the oscilloscope through analog output channels.

Fig. 20(a) compares the performance of the conventional droop and FOD droop controllers under load disturbance event. In the beginning, the system is controlled with the conventional droop controller with  $m_p = 7.85 \times 10^{-3}$  rad/s/W and a nominal voltage  $V_{nom} = 75$  V while all switches are closed. Then, the resistance bank of load 2 is removed by opening  $SW_2$  which causes an overshoot of 30% in the active power of inverter 2 and undershoot of 55% for inverters 1 and 2. After  $\approx 4$  s, the system is subjected to a load-in event when the resistive bank of load 2 is reconnected. This resulted in an overshoot of 20% in inverter 2. After  $\approx 4$  s, FOD droop is turned on with orders  $\alpha = 1.5$  and  $\beta = 1.3$  and derivative droop gains  $m_d = 0.00035$  rad/W and  $n_d = 0.0005$  V·s/VAR, then after  $\approx 2.5$  s, the same load disturbance is performed. However, the load-out event overshoot is reduced to  $\approx 12.5\%$  for inverter 2 and the undershoot is reduced to 40% for inverter 2. During the load-in event under the FOD controller, the overshoot of inverter 2 is reduced to 15%. Another observation is that the FOD droop has achieved more transient power-sharing than the conventional droop controller, where the power is almost equally shared even during transient time.

Another experimental case study is made at  $m_p = 6.28 \times 10^{-3}$  rad/s/W and  $V_{nom} = 100$  V while  $SW_3$  is open. As shown in Fig. 20(b), the conventional droop controller gives an oscillatory active power response. However, when the FOD droop is turned on with  $\alpha = 1.5$  and  $m_d = 0.00035$  rad/W and  $n_d = 0$  V·s/VAR, the high-frequency oscillations disappear. This verifies the stability analysis results and shows the stabilization effect of the FOD droop controller.

## VII. CONCLUSION

This article proposed the FOD droop controller to improve the dynamic performance of the well-known IOD droop controller

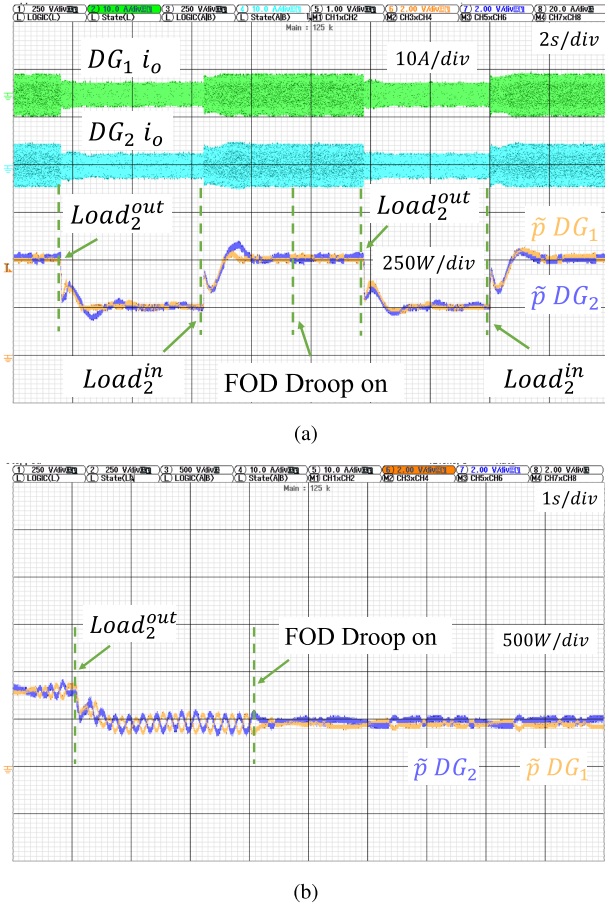


Fig. 20. Experimental comparison between conventional droop control and FOD droop control. (a) Conventional droop followed by FOD droop at load disturbance. (b) Stabilizing effect of FOD droop.

used in inverter-based islanded MGs. An efficient method was developed to implement biproper transfer function approximations of the FO operator inside state space models dominated with IO states. Then, this method was used to develop the complete SSM of the MG under FOD droop control. Exhaustive search results of the derivative droop gains showed the potential of the proposed controller to enhance the power-sharing dynamics even at the same value of the largest real part of the eigenvalues. After adding extra LPFs to increase the tunability of the IOD droop, an optimization procedure was proposed to tune the parameters of both the IOD and FOD droop controllers. The simulation results of the tuned controllers in a benchmark MG showed the merit of the FOD droop at significantly reducing the overshoot, the ST, and the oscillatory response at several contingency events, including large load disturbance. The controllers were also tested at a reconfiguration scenario of another MG where the network undergoes two consecutive transitions from radial to meshed to radial again. The FOD droop also showed reduced overshoot and reduced oscillation of the power transient, especially during the first event, which is known to degrade the relative stability of MGs. A comprehensive sensitivity analysis was performed and showed the robustness of the proposed controller under parameter uncertainty and multiple disturbance

events. Experimental validations on a laboratory scale two DG MG showed the applicability and efficacy of the proposed FOD droop controller in improving the power-sharing dynamics at load disturbance events. In summary, it is evident that the extra degrees of freedom provided by the FOD droop can be used to improve the dynamic power-sharing performance of parallel-operated inverters in islanded MGs as proven in small signal analysis, verified by simulations, and validated on a lab-scale MG. The proposed power-sharing controller, FOD droop, can later be used as a stabilizing component in a larger control scheme targeting other MG issues like unbalanced operation, load harmonic sharing, etc.

#### ACKNOWLEDGMENT

The authors would like to thank the contribution of Khalifa University's high-performance computing and research computing facilities to the results of this research.

#### APPENDIX

The parameters of the system in Section IV are [42]:  $R_f = 0.1 \Omega$ ,  $L_f = 1.35 \text{ mH}$ ,  $C_f = 50 \mu\text{F}$ ,  $R_C = 0.03 \Omega$ ,  $L_C = 0.35 \text{ mH}$ ,  $R_{line1} = 0.23 \Omega$ ,  $L_{line1} = 0.35 \text{ mH}$ ,  $R_{line2} = 0.35 \Omega$ ,  $L_{line2} = 1.85 \text{ mH}$ ,  $load1 = load2 = (22.5 + j6) \text{ kVA}$ ,  $m_p = 6.28 \times 10^{-4} \text{ rad/s/W}$ ,  $n_q = 1.3 \times 10^{-3} \text{ V/VAr}$ ,  $K_{pc} = 10.5$ ,  $K_{ic} = 16 \times 10^3$ ,  $K_{pv} = 0.05$ ,  $K_{iv} = 390$ ,  $\omega_c = 31.41 \text{ rad/s}$ ,  $F = 0.75$ ,  $\omega_{nom} = 314.15 \text{ rad/s}$ .

The parameters of Section IV-E are as follows. The line impedance data are  $(0.1 + j0.08)\Omega$ ,  $(0.2 + j0.35)\Omega$ ,  $(0.15 + j0.19)\Omega$ ,  $(0.2 + j0.10)\Omega$ ,  $(0.18 + j0.25)\Omega$ , and  $(0.15 + j0.16)\Omega$ , for lines  $L_1$  through  $L_6$ , respectively. The load data are  $(13.0 + j1.5) \text{ kVA}$ ,  $(1.0 + j0.3) \text{ kVA}$ ,  $(5.0 + j3.0) \text{ kVA}$ ,  $(11.5 + j2.0) \text{ kVA}$ ,  $(1.5 + j0.1) \text{ kVA}$ , and  $(17.0 + j2.0) \text{ kVA}$  for loads  $Ld_1$  through  $Ld_6$ , respectively.

The parameters of the experiment in Section VI are as follows.  $L_{line} = 0.8 \text{ mH}$ ,  $L_f = 2.5 \text{ mH}$ ,  $C_f = 30 \mu\text{F}$ ,  $L_C = 1.6 \text{ mH}$ ,  $R_{load1} = 40 \Omega$ ,  $R_{load2} = 35 \Omega$ ,  $V_{DC} = 500 \text{ V}$ ,  $K_{pc} = 0.5$ ,  $K_{ic} = 500$ ,  $K_{pv} = 0.01$ ,  $K_{iv} = 0.1$ ,  $F = 0.75$ . The approximated and discretized FOD implementations are given as follows:

$$s^{1.5-1} = s^{0.5} \approx \frac{96.11(s + 500.1)(s + 28.99)(s + 1.066)}{(s + 3155)(s + 116)(s + 6.725)} \rightarrow \frac{89.989(1 - 0.99995z^{-1})(1 - 0.9986z^{-1})(1 - 0.9753z^{-1})}{(1 - 0.9997z^{-1})(1 - 0.9942z^{-1})(1 - 0.8538z^{-1})} \quad (35a)$$

$$s^{1.3-1} = s^{0.3} \approx \frac{30.446(s + 7482)(s + 425)(s + 19.03)}{(s + 2.167e04)(s + 970.5)(s + 55.13)} \rightarrow \frac{23.107(1 - 0.999z^{-1})(1 - 0.979z^{-1})(1 - 0.6849z^{-1})}{(1 - 0.9972z^{-1})(1 - 0.9526z^{-1})(1 - 0.2971z^{-1})} \quad (35b)$$

#### REFERENCES

- [1] A. K. Sahoo, K. Mahmud, M. Crittenden, J. Ravishankar, S. Padmanaban, and F. Blaabjerg, "Communication-less primary and secondary control in inverter-interfaced AC microgrid: An overview," *IEEE Trans. Emerg. Sel. Topics Power Electron.*, vol. 9, no. 5, pp. 5164–5182, Oct. 2020.



- [2] J. Chen, D. Yue, C. Dou, L. Chen, S. Weng, and Y. Li, "A virtual complex impedance based  $P-V$  droop method for parallel-connected inverters in low-voltage AC microgrids," *IEEE Trans. Ind. Informat.*, vol. 17, no. 3, pp. 1763–1773, Mar. 2021.
- [3] M. B. Abdelghany, A. Al-Durra, and F. Gao, "A coordinated optimal operation of a grid-connected wind-solar microgrid incorporating hybrid energy storage management systems," *IEEE Trans. Sustain. Energy*, vol. 15, no. 1, pp. 39–51, Jan. 2024.
- [4] J. Yang, C. K. Tse, and D. Liu, "Nonlinear behavior and reduced-order models of islanded microgrid," *IEEE Trans. Power Electron.*, vol. 37, no. 8, pp. 9212–9225, Aug. 2022.
- [5] Y. Shan, J. Hu, K. W. Chan, and S. Islam, "A unified model predictive voltage and current control for microgrids with distributed fuzzy cooperative secondary control," *IEEE Trans. Ind. Informat.*, vol. 17, no. 12, pp. 8024–8034, Dec. 2021.
- [6] J. Liu, Y. Miura, H. Bevrani, and T. Ise, "Enhanced virtual synchronous generator control for parallel inverters in microgrids," *IEEE Trans. Smart Grid*, vol. 8, no. 5, pp. 2268–2277, Sep. 2017.
- [7] Z. Shuai, W. Huang, Z. J. Shen, A. Luo, and Z. Tian, "Active power oscillation and suppression techniques between two parallel synchronverters during load fluctuations," *IEEE Trans. Power Electron.*, vol. 35, no. 4, pp. 4127–4142, Apr. 2020.
- [8] M. Chen, D. Zhou, and F. Blaabjerg, "Active power oscillation damping based on acceleration control in paralleled virtual synchronous generators system," *IEEE Trans. Power Electron.*, vol. 36, no. 8, pp. 9501–9510, Aug. 2021.
- [9] S. Fu, Y. Sun, L. Li, Z. Liu, H. Han, and M. Su, "Power oscillation suppression of multi-VSG grid via decentralized mutual damping control," *IEEE Trans. Ind. Electron.*, vol. 69, no. 10, pp. 10202–10214, Oct. 2022.
- [10] H. Yin, S. Wang, and Z. Zhou, "Synchronverters with a virtual oscillator to attenuate power oscillations," *IEEE J. Emerg. Sel. Topics Power Electron.*, early access, Nov. 6, 2022, doi: [10.1109/JESTPE.2023.3329010](https://doi.org/10.1109/JESTPE.2023.3329010).
- [11] J. Lin, S. Liu, M. Tian, M. Huang, and G. Wang, "Power oscillation suppression of multi-VSG based on both consensus and model predictive control," *Int. J. Elect. Power Energy Syst.*, vol. 155, 2024, Art. no. 109459.
- [12] S. Chen et al., "Active power oscillation suppression and dynamic performance improvement for multi-VSG grids based on consensus control via COI frequency," *Int. J. Elect. Power Energy Syst.*, vol. 147, 2023, Art. no. 108796.
- [13] Z. Wang et al., "Active power oscillation suppression based on decentralized transient damping control for parallel virtual synchronous generators," *IEEE Trans. Smart Grid*, vol. 14, no. 4, pp. 2582–2592, Jul. 2022.
- [14] B. Wang and G. Verbič, "Stability analysis of low-voltage distribution feeders operated as islanded microgrids," *IEEE Trans. Smart Grid*, vol. 12, no. 6, pp. 4681–4689, Nov. 2021.
- [15] D. K. Dheer, V. A.S., O. V. Kulkarni, and S. Doolla, "Improvement of stability margin of droop-based islanded microgrids by cascading of lead compensators," *IEEE Trans. Ind. Appl.*, vol. 55, no. 3, pp. 3241–3251, May/Jun. 2019.
- [16] G. Raman and J. C.-H. Peng, "Mitigating stability issues due to line dynamics in droop-controlled multi-inverter systems," *IEEE Trans. Power Syst.*, vol. 35, no. 3, pp. 2082–2092, May 2020.
- [17] M. Eskandari and A. V. Savkin, "A critical aspect of dynamic stability in autonomous microgrids: Interaction of droop controllers through the power network," *IEEE Trans. Ind. Informat.*, vol. 18, no. 5, pp. 3159–3170, May 2022.
- [18] H. Safamehr, I. Izadi, and J. Ghaisari, "Robust VI droop control of grid-forming inverters in the presence of feeder impedance variations & nonlinear loads," *IEEE Trans. Ind. Electron.*, vol. 71, no. 1, pp. 504–512, Jan. 2024.
- [19] J. Kweon, H. Jing, Y. Li, and V. Monga, "Small-signal stability enhancement of islanded microgrids via domain-enriched optimization," *Appl. Energy*, vol. 353, 2024, Art. no. 122172.
- [20] S. Harasis, "Controllable transient power sharing of inverter-based droop controlled microgrid," *Int. J. Elect. Power Energy Syst.*, vol. 155, 2024, Art. no. 109565.
- [21] M. Aquib, N. Parth, S. Doolla, and M. C. Chandorkar, "An adaptive droop scheme for improving transient and steady-state power sharing among distributed generators in islanded microgrids," *IEEE Trans. Ind. Appl.*, vol. 59, no. 4, pp. 5136–5148, Jul./Aug. 2023.
- [22] J. M. Guerrero, L. G. De Vicuna, J. Matas, M. Castilla, and J. Miret, "A wireless controller to enhance dynamic performance of parallel inverters in distributed generation systems," *IEEE Trans. Power Electron.*, vol. 19, no. 5, pp. 1205–1213, Sep. 2004.
- [23] J. M. Guerrero, J. Matas, L. G. de Vicuna, M. Castilla, and J. Miret, "Decentralized control for parallel operation of distributed generation inverters using resistive output impedance," *IEEE Trans. Ind. Electron.*, vol. 54, no. 2, pp. 994–1004, Apr. 2007.
- [24] Y. A.-R. I. Mohamed and E. F. El-Saadany, "Adaptive decentralized droop controller to preserve power sharing stability of paralleled inverters in distributed generation microgrids," *IEEE Trans. Power Electron.*, vol. 23, no. 6, pp. 2806–2816, Nov. 2008.
- [25] Y. A.-R. I. Mohamed, H. H. Zeineldin, M. M. A. Salama, and R. Seethapathy, "Seamless formation and robust control of distributed generation microgrids via direct voltage control and optimized dynamic power sharing," *IEEE Trans. Power Electron.*, vol. 27, no. 3, pp. 1283–1294, Mar. 2012.
- [26] J. Chen, L. Wang, L. Diao, H. Du, and Z. Liu, "Distributed auxiliary inverter of urban rail train-load sharing control strategy under complicated operation condition," *IEEE Trans. Power Electron.*, vol. 31, no. 3, pp. 2518–2529, Mar. 2016.
- [27] B. Hamad, A. Al-Durra, T. H. M. EL-Fouly, and H. H. Zeineldin, "Economically optimal and stability preserving hybrid droop control for autonomous microgrids," *IEEE Trans. Power Syst.*, vol. 38, no. 1, pp. 934–947, Jan. 2023.
- [28] A. Lasheen, M. E. Ammar, H. H. Zeineldin, A. Al-Durra, M. F. Shaaban, and E. El-Saadany, "Assessing the impact of reactive power droop on inverter based microgrid stability," *IEEE Trans. Energy Convers.*, vol. 36, no. 3, pp. 2380–2392, Sep. 2021.
- [29] M. V. Kazemi, S. J. Sadati, and S. A. Gholamian, "Adaptive frequency control of microgrid based on fractional order control and a data-driven control with stability analysis," *IEEE Trans. Smart Grid*, vol. 13, no. 1, pp. 381–392, Jan. 2022.
- [30] J. A. T. Machado and V. Kiryakova, *Recent History of the Fractional Calculus: Data and Statistics*. Berlin, Germany: De Gruyter, 2019, pp. 1–22.
- [31] Y. Wang, G. Zhao, C. Zhou, M. Li, and Z. Chen, "Lithium-ion battery optimal charging using moth-flame optimization algorithm and fractional-order model," *IEEE Trans. Transport. Electrification*, vol. 9, no. 4, pp. 4981–4989, Dec. 2023.
- [32] S. Adigintla, M. V. Aware, and N. Arun, "Fractional order transfer function identification of six-phase induction motor using dual chirp signal," *IEEE Trans. Emerg. Sel. Topics Power Electron.*, vol. 11, no. 5, pp. 5183–5194, Oct. 2023.
- [33] Y. Chu, S. Hou, C. Wang, and J. Fei, "Recurrent-neural-network-based fractional order sliding mode control for harmonic suppression of power grid," *IEEE Trans. Ind. Informat.*, vol. 19, no. 10, pp. 9979–9990, Oct. 2023.
- [34] S. Das and I. Pan, "On the mixed  $H_2/H_\infty$  loop-shaping tradeoffs in fractional-order control of the AVR system," *IEEE Trans. Ind. Informat.*, vol. 10, no. 4, pp. 1982–1991, Nov. 2014.
- [35] P. Xu, X. Hu, B. Liu, T. Ouyang, and N. Chen, "Hierarchical estimation model of state-of-charge and state-of-health for power batteries considering current rate," *IEEE Trans. Ind. Informat.*, vol. 18, no. 9, pp. 6150–6159, Sep. 2022.
- [36] Z. Li, Z. Li, H. Xu, X. Zhang, and C.-Y. Su, "Development of a butterfly fractional-order backlash-like hysteresis model for dielectric elastomer actuators," *IEEE Trans. Ind. Electron.*, vol. 70, no. 2, pp. 1794–1801, Feb. 2023.
- [37] M. Ö. Efe, "Fractional order systems in industrial automation—a survey," *IEEE Trans. Ind. Informat.*, vol. 7, no. 4, pp. 582–591, Nov. 2011.
- [38] D. Xue, *FOTF Toolbox for Fractional-Order Control Systems*. Berlin, Germany: De Gruyter, 2019, pp. 237–266.
- [39] S. Fu, Y. Sun, L. Li, Z. Liu, H. Han, and M. Su, "Power oscillation suppression in multi-VSG grid by adaptive virtual impedance control," *IEEE Syst. J.*, vol. 16, no. 3, pp. 4744–4755, Sep. 2022.
- [40] W. Krajewski and U. Viaro, "A method for the integer-order approximation of fractional-order systems," *J. Franklin Inst.*, vol. 351, no. 1, pp. 555–564, 2014.
- [41] S. Sen and V. Kumar, "Microgrid modelling: A comprehensive survey," *Annu. Rev. Control*, vol. 46, pp. 216–250, 2018.
- [42] N. Pogaku, M. Prodanovic, and T. C. Green, "Modeling, analysis and testing of autonomous operation of an inverter-based microgrid," *IEEE Trans. Power Electron.*, vol. 22, no. 2, pp. 613–625, Mar. 2007.
- [43] M. S. Tavazoei and M. Tavakoli-Kakhki, "Minimal realizations for some classes of fractional order transfer functions," *IEEE Trans. Emerg. Sel. Topics Circuits Syst.*, vol. 3, no. 3, pp. 313–321, Sep. 2013.
- [44] *IEEE Standard for Interconnection and Interoperability of Distributed Energy Resources With Associated Electric Power Systems Interfaces*, IEEE Std 1547-2018 (Revision of IEEE Std 1547-2003), 2018, pp. 1–138.

- [45] W. Peres, F. C. Coelho, and J. N. Costa, "A pole placement approach for multi-band power system stabilizer tuning," *Int. Trans. Elect. Energy Syst.*, vol. 30, no. 10, 2020, Art. no. e12548.
- [46] Y. L. Abdel-Magid and M. A. Abido, "Optimal multiobjective design of robust power system stabilizers using genetic algorithms," *IEEE Trans. Power Syst.*, vol. 18, no. 3, pp. 1125–1132, Aug. 2003.
- [47] A. Faramarzi, M. Heidarinejad, S. Mirjalili, and A. H. Gandomi, "Marine predators algorithm: A nature-inspired metaheuristic," *Expert Syst. Appl.*, vol. 152, 2020, Art. no. 113377.
- [48] B. B. Johnson, M. Sinha, N. G. Ainsworth, F. Dörfler, and S. V. Dhople, "Synthesizing virtual oscillators to control islanded inverters," *IEEE Trans. Power Electron.*, vol. 31, no. 8, pp. 6002–6015, Aug. 2016.
- [49] D. Çelik and M. E. Meral, "A coordinated virtual impedance control scheme for three phase four leg inverters of electric vehicle to grid (V2G)," *Energy*, vol. 246, 2022, Art. no. 123354.
- [50] D. K. Dheer, O. V. Kulkarni, S. Doolla, and A. K. Rathore, "Effect of reconfiguration and meshed networks on the small-signal stability margin of droop-based islanded microgrids," *IEEE Trans. Ind. Appl.*, vol. 54, no. 3, pp. 2821–2833, May/Jun. 2018.



**Amr M. AbdelAty** (Senior Member, IEEE) received the B.Sc. in electronics and electrical communication engineering, in 2011, the M.Sc. and the Ph.D. degrees in engineering mathematics in 2016 and 2021, all from Faculty of Engineering, Fayoum University, Fayoum, Egypt.

He was an Assistant Lecturer with the Department of Engineering Mathematics, Fayoum University, Fayoum, Egypt, between 2013 and 2021. He has been an Assistant Professor of engineering mathematics with Fayoum University since 2021. He was a Postdoctoral fellow with APEC, Khalifa University, Abu Dhabi, UAE, in 2022 and 2023. He has authored or coauthored more than 50 publications, including journal articles, conference papers, and book chapters. His main research interests are fractional-order modeling and control of circuits and systems.

Prof. AbdelAty is a Reviewer for many international Journals. He is the winner of the best Ph.D. thesis award from Fayoum University, Egypt, for the year 2021, for his thesis entitled "Fractional-order Modeling of Energy Systems." He was a recipient of the Oliviu Gherman Award for his contributions to applying fractional calculus to solving real-world problems during OCMFCA-2020.

He is currently an Assistant Professor with the Department of Electrical Engineering and Computer Science, Khalifa University, Abu Dhabi, UAE. He is also the Associate Provost for Research with Khalifa University. He has authored or coauthored more than 340 scientific articles in top-tier journals and refereed international conference proceedings. His research interests are applications of control and estimation theory on power systems stability, micro and smart grids, renewable energy systems and integration, and process control.

Prof. Al-Durra has supervised/co-supervised more than 30 Ph.D./Master's students. He is leading the Energy Systems Control & Optimization Lab under the Advanced Power & Energy Center, an Editor for IEEE TRANSACTIONS ON SUSTAINABLE ENERGY AND IEEE POWER ENGINEERING LETTERS, and Associate Editor for IEEE TRANSACTIONS ON INDUSTRY APPLICATIONS.



**Ahmed Al-Durra** (Senior Member, IEEE) received the B.Sc., M.Sc., and Ph.D. degrees in electrical & computer engineering from Ohio State University, Columbus, OH, USA, in 2005, 2007, and 2010, respectively.

He is a Professor with the Electrical Engineering and Computer Science Department, Khalifa University, Abu Dhabi, UAE. He is also the Associate Provost for Research with Khalifa University. He has authored or coauthored more than 340 scientific articles in top-tier journals

and refereed international conference proceedings. His research interests are applications of control and estimation theory on power systems stability, micro and smart grids, renewable energy systems and integration, and process control.

Prof. Al-Durra has supervised/co-supervised more than 30 Ph.D./Master's students. He is leading the Energy Systems Control & Optimization Lab under the Advanced Power & Energy Center, an Editor for IEEE TRANSACTIONS ON SUSTAINABLE ENERGY AND IEEE POWER ENGINEERING LETTERS, and Associate Editor for IEEE TRANSACTIONS ON INDUSTRY APPLICATIONS.



**Hatem H. Zeineldin** (Senior Member, IEEE) received the B.Sc. and M.Sc. degrees in electrical engineering from Cairo University, Giza, Egypt, in 1999 and 2002, respectively, and the Ph.D. degree in electrical and computer engineering from the University of Waterloo, Waterloo, ON, Canada, in 2006.

He was with Smith and Andersen Electrical Engineering Inc., North York, ON, USA, where he was involved in projects involving distribution system designs, protection, and distributed generation. He was a Visiting Professor with the Massachusetts Institute of Technology, Cambridge, MA, USA. He is currently with Khalifa University, Abu Dhabi, UAE, and on leave from the Faculty of Engineering, Cairo University. His current research interests include distribution system protection, distributed generation, and microgrids.



**Saikrishna Kanukollu** (Member, IEEE) received the B.Tech. degree in electrical and electronics engineering from Jawaharlal Nehru Technological University, Hyderabad, India, in 2008, and the M.Tech. degree in power electronics and power systems from the Indian Institute of Technology Bombay, Maharashtra, India, in 2010.

From 2010 to 2011, he was a Power System Application (SCADA/EMS) Development Engineer at the ABB India Development Center, Bengaluru. He joined The Petroleum Institute (now part of Khalifa University), Abu Dhabi, UAE, in 2012 as a Research Engineer to work on various power electronics projects related to the national oil & gas industry. From 2016 to 2021, he held the position of Research Laboratory Engineer with ADNOC Research and Innovation Centre, Khalifa University (KU), where he played an instrumental role in the establishment of one of the UAE's largest research centers for power electronics and power systems. During this tenure, he served in various capacities, overseeing the development of research facilities and the construction of hardware prototypes for both academia and industry (including power electronics, motor drives, renewable energy systems, and enhanced oil recovery systems using AI hardware). Since 2021, he has been working as a Full-Time Research Engineer with the Energy Systems, Control, and Optimization (ESCO) lab at KU, focusing on research in microgrids and the integration of renewable energy systems. His research interests include high-density power converters, digital control, large-scale simulation of power systems, and hardware-in-the-loop simulation.



**Ehab F. El-Saadany** (Fellow, IEEE) He was born in Cairo, Egypt, in 1964. He received the B.Sc. and M.Sc. degrees in electrical engineering from Ain Shams University, Cairo, Egypt, in 1986 and 1990, respectively, and the Ph.D. degree in electrical engineering from the University of Waterloo, Waterloo, ON, Canada, in 1998. He was a Professor with the ECE Department, University of Waterloo, till 2019, where he was the Director of the Power M.Eng. program between 2010 and 2015. Currently, he is a Professor with

the Department of Electrical Engineering and Computer Science and the Director of the Advanced Power and Energy Research Center (APEC), Khalifa University, UAE. He is an Internationally recognized expert in the area of sustainable energy integration and smart distribution systems. He is a Registered Professional Engineer in the Province of Ontario. His research interests include smart grid operation and control, microgrids, transportation electrification, self-healing, cyber-physical security of smart grids, protection, power quality, and embedded generation. He has contributed in distributed generation planning, operation and control.